

This manuscript is a preprint and has been submitted to Geochemistry, Geophysics, Geosystems. It has not undergone peer-review. Subsequent versions of this manuscript may have different content as a result of the review process.

Demise of the Barra Honda carbonate shoal (Costa Rica) at the Paleocene-Eocene boundary linked to climate change and forearc tectonics

Goran Andjić^{1*}, Claudia Baumgartner-Mora¹, Peter O. Baumgartner¹, Maria Rose Petrizzo², Torsten Vennemann³, André N. Paul^{4,5}, Valentin Lorenzo¹

¹*Institute of Earth Sciences, University of Lausanne, Géopolis, 1015 Lausanne, Switzerland*

²*Dipartimento di Scienze della Terra, Università degli Studi di Milano, Milano, Italy*

³*Institute of Earth Surface Dynamics, University of Lausanne, Géopolis, 1015 Lausanne, Switzerland*

⁴*Department of Earth Sciences, University of Geneva, Section of Earth and Environmental Sciences, Geneva, Switzerland*

⁵*Institute of Geosciences, Goethe University Frankfurt, Frankfurt, Germany*

*Corresponding author: goran.andjic@unil.ch

Key Points

- U-Pb age, biostratigraphic, and stable isotope compositions show that the Barra Honda carbonate shoal ended at the Paleocene-Eocene boundary
- Ocean acidification and increased detrital/nutrient influx may be the primary causes of the demise
- High subsidence rates of the forearc basin during the early Eocene terminated the shallow carbonate sedimentation

Abstract

The latest Cretaceous(?)–Paleocene Barra Honda Formation represents one of the largest carbonate shoals (>900 km², 350 m thick) of the convergent margin of Costa Rica. Although the mode of formation of the carbonate shoal is well understood, how environmental and tectonic factors interacted to cause its demise near the Paleocene-Eocene boundary remains poorly constrained. Stable isotopic, biostratigraphic, mineralogical, and geochronologic analyses from the Barra Honda Formation and overlying siliceous Buenavista Formation provide new constraints on the timing and causes of the demise of the carbonate shoal. We report one new U–Pb zircon chemical abrasion, isotope dilution, thermal ionization mass spectrometry date (56.30 Ma ± 0.13 Ma, 2σ) obtained from an ash-rich layer at the boundary between the two formations. The sharp transition from Barra Honda massive limestones to Buenavista marl-chert alternations coincides with a negative shift in carbon isotope ($\delta^{13}\text{C}_{\text{carb}}$) values of about 3 to 5 ‰ and a 50 % decrease in carbonate contents. The timing of the combined lithological-mineralogical-isotopic change is coeval with the Paleocene-Eocene Thermal Maximum (PETM, 56 Ma). The onset of clay-rich sedimentation is consistent with a PETM-related increase of terrestrial influx of nutrients and detrital particles, which promoted eutrophication and decreased light availability in the photic zone. Combined with seawater acidification and warming, these environmental parameters were fatal to carbonate-producing benthic communities of Barra Honda. High subsidence rates of the

48 forearc basin and renewed arc volcanic activity must have closely followed the cessation of shallow
49 carbonate production, preventing further formation of the carbonate shoal.

50

51 **Plain Language Summary**

52

53 The Barra Honda Formation in Costa Rica is a large area of carbonate rocks formed during the latest
54 Cretaceous(?)–Paleocene interval. We wanted to understand why this carbonate shoal, which was
55 formed by a favorable combination of environmental and tectonic factors, disappeared around the
56 Paleocene–Eocene boundary. We studied different aspects, i.e., stable isotopes, microfossils, minerals,
57 and ages of rocks from the Barra Honda Formation and the overlying Buenavista Formation. We present
58 a new age date from zircons recovered from an ash layer between these formations, showing that the
59 lithological change happened around 56 million years ago. At that time, there was a sudden shift in the
60 types of sedimentary rocks deposited and in their carbon isotope values. This change coincides with a
61 significant global event called the Paleocene–Eocene Thermal Maximum (PETM), known for causing
62 environmental upheavals like ocean warming and increased ocean water acidity. These factors caused
63 more nutrients to flow in from land and reduced light in the seawater, and likely led to the decline of
64 benthic communities in the Barra Honda carbonate shoal. Additionally, the basin where these carbonate
65 rocks formed started sinking rapidly after the PETM event, preventing the shoal from recovering.

66

67 **1. Introduction**

68

69 Oceanic Central America is composed of a puzzle of oceanic plateau and arc terranes that extend
70 between the North America-derived, continental Chortis terrane, and the South American plate
71 outcropping in the Columbian Andes (Figure 1a; Rogers et al., 2007; Baumgartner et al., 2008; Buchs
72 et al., 2010; Andjić et al., 2019a, 2019b). No older continental basement is known to occur in these
73 southern Central American terranes, that form the trailing edge of the Caribbean Plate (Mann, 2007;
74 Pindell & Kennan, 2009). Sedimentation along the Central American convergent margin was dominated
75 by arc-derived deep-water volcano-detrital deposits throughout the Late Mesozoic-Cenozoic
76 (Escalante, 1991; Alvarado et al., 2007). Nevertheless, shallow-water carbonates do occur
77 (Baumgartner-Mora & Baumgartner, 2016) and are characterized by: (i) sudden appearance and
78 disappearance of conditions for chlorozoan carbonate production; (ii) modest size (1-100 km wide);
79 and (iii) a geologically short period (1-10 Ma). These “punctuated chlorozoan carbonates”
80 (Baumgartner-Mora et al., 2019) occur all along the Mid-American convergent margin and consist of
81 short-lived carbonate banks and buildups, interstratified in generally deep-water turbiditic fore- and
82 back-arc series. Hence, punctuated chlorozoan carbonates formed under overall unfavorable conditions:
83 (i) a high input of suspended detrital particles was produced by tropical weathering of emerged oceanic
84 terranes and superposed volcanic edifices, as well as airborne ashes from active volcanoes; (ii) the rise
85 into the photic zone of any oceanic substrate suitable for punctuated chlorozoan carbonates was
86 controlled either by accretion tectonics or by intra-oceanic volcanism (oceanic islands, plateaus, arcs).
87 Carbonate production in long-lived (10-60 Ma), large carbonate shelves set along passive margins, is
88 thought to be controlled primarily by paleoclimate and eustatic sea level change (e.g., Kemp & Sadler,
89 2014). In contrast, punctuated chlorozoan carbonates are the biotic response to convergent-margin
90 endogenic processes, such as tectonic uplift related to the subduction/accretion of topographic relief on
91 the subducting plate, that may result in a temporary arc gap (Andjić et al., 2018a, 2018b) and thus a
92 reduction of detrital discharge (Andjić et al., 2019a).

93

94 The uppermost Cretaceous(?)–Paleocene Barra Honda Formation (Fm.; Dengo, 1962), located in the
95 Guanacaste Province of Costa Rica (Figure 1b), largely built of chloralgal carbonate mud, is a good
96 example of a short-lived, moderately-sized (originally >900 km²) chlorozoan carbonate shoal. Its age
97 and stratigraphic setting were enigmatic for a long time, because of the scarcity of age-diagnostic fossils
98 and its position sandwiched unconformably between Upper Cretaceous and Eocene deep-water clastic

99 formations. Jaccard et al. (2001) re-mapped the formation and described occurrences of *Ranikothalia*
100 *catenula* group and *Neodiscocyclina barkeri* from the upper Barra Honda Fm. and assigned it to a late
101 Paleocene to early Eocene age. Facies models for the upper Barra Honda Fm. were proposed in Jaccard
102 et al. (2001) and Baumgartner-Mora and Baumgartner (2016). The latter authors revised the systematics
103 of *Ranikothalia* and gave a general account of upper Paleocene carbonates of Costa Rica and western
104 Panama.

105
106 This study examines the stratigraphic top of the Barra Honda Fm. and the overlying pelagic cherts and
107 limestones (Buenavista Fm.) that crop out in an active quarry 4.5 km east of the town of Nicoya (Figure
108 1b). In coeval, more distal, deep-water sections a pelagic cherty limestone series (Buenavista Fm.)
109 records a break in the detrital forearc sedimentation between the underlying predominantly basaltic
110 forearc turbidites (Curú Fm.) and the overlying, more andesitic turbidites of the Descartes Fm.
111 (Baumgartner et al., 1984). The sediment petrologic change has been known for a long time (Lundberg,
112 1982) and the break has been interpreted by us as a possible regional, temporary arc gap between a
113 primitive and a more evolved island arc (Andjić et al., 2018a). The birth and growth of the Barra Honda
114 carbonate shoal has been previously discussed as a biotic response to the lack and/or bypassing of
115 detrital input during the arc gap and uplift of the proximal forearc basin (Baumgartner-Mora &
116 Baumgartner, 2016; Andjić et al., 2018a). In this study, we combine carbon stable isotope stratigraphy,
117 bulk mineralogy analysis, zircon dating, and micropaleontology to test whether the sudden demise of
118 the Barra Honda Fm. near the Paleocene–Eocene boundary may be primarily controlled by climate
119 change during the PETM.

120
121 The abrupt shift from carbonate-rich to carbonate-poor layers—such as the Barra Honda–Buenavista
122 boundary—has been described in marine PETM sections around the world. Centimeter- to meter-sized
123 clay-rich layers coincide with the onset of the PETM, with examples from onshore sections (Schmitz
124 et al., 2001; Aubry et al., 2007; Giusberti et al. 2007; Bralower et al., 2018) and offshore drillholes
125 (Lyle et al., 2002; Zachos et al., 2004; Colosimo et al., 2006; Borneman et al., 2014; Penman, 2016;
126 Wade et al., 2020). The interruption of carbonate-rich sedimentation in deep seas has been interpreted
127 as the result of ocean acidification that accompanied the rapid release of large amounts of CO₂ (e.g.,
128 Dickens et al., 1997; Zachos et al., 2005; Zeebe & Zachos, 2007; Penman et al., 2014; Babila et al.,
129 2018). The decrease or absence of carbonate accumulation and preservation in deep-water settings was
130 primarily associated with the shallowing of the lysocline and carbonate compensation depth (Zachos et
131 al., 2005; Gibbs et al., 2010; Murphy et al., 2010). The shallow-water, tectonically active, arc-proximal
132 setting of the Barra Honda carbonate shoal requires a discussion on the interplay of local and global
133 (e.g., ocean acidification) factors in its demise at the Paleocene–Eocene boundary.

134 135 *1.1. Margin response to rough crust subduction*

136
137 The subduction of bathymetric reliefs influences the structural and magmatic evolution of convergent
138 margins (Cloos, 1993). Whether accretion occurs or not, the primary response of the upper plate is to
139 accommodate the colliding object by kilometeric surface uplift in the forearc (Spikings & Simpson,
140 2014). Hence, the amplitude of vertical tectonic motions may be of up to two orders of magnitude higher
141 than eustatic variations (Gardner et al., 2013). Short-lived, shallow-water and sub-aerial environments
142 appear in the inner and/or outer forearc and replace previous long-lived, deep-water domains (Dorobek,
143 2008). Except in the case of stationary subduction of an aseismic ridge or hotspot track (~1000 km
144 length scale), the duration of forearc uplift is generally shorter than 5 Ma (Meffre & Crawford, 2001;
145 Tetreault & Buitter, 2012; Vogt & Gerya, 2014). Once the colliding bathymetric feature is subducted,
146 the forearc seafloor subsides to its previous water depth; if rough crust subduction caused tectonic
147 erosion of the upper plate, the forearc basin subsides to deeper water depths than in its pre-collisional
148 state (von Huene & Suess, 1988).

149

150 A possible secondary response of the upper plate to the collision of bathymetric relief is cessation of
151 the volcanic activity, which occurs after the initial stage of collision at shallow depths. Spatial gaps in
152 volcanism develop when the leading edge of the object, or its remaining root, reaches greater depth
153 where it may promote flat slab subduction, slab break-off, or modification of dehydration processes in
154 the mantle wedge (McGeary et al., 1985; Rosenbaum & Mo, 2011; Bishop et al., 2017). In the latter
155 case, considering orthogonal convergence rates comprised between ~3.5 and 12 cm/yr (e.g., Young et
156 al., 2019), volcanic arc cessation in response to the arrival of the object at the depth of major slab
157 dehydration and arc magmagenesis (~100 km; Ranero et al., 2005) may occur between ~0.8 and 3 Ma
158 after the onset of collision. If the object is long enough (>100 km), a magmatic lull occurs while surface
159 uplift is sustained by the subduction of the object trailing edge.

160
161 The identification of arc gaps in ancient volcanic formations is uncertain, because igneous rocks are
162 often discontinuously preserved. Drawing mainly on examples from Central America, Andjić et al.
163 (2018a) have recently shown that forearc sedimentary rocks can record lulls in the magmatic history of
164 arcs (Figure 2). In particular, the abrupt interruption of volcanoclastic sedimentation in forearc basins
165 and its replacement by pelagic sedimentation indicate a demise in the production of arc-derived
166 material. After the collision of the bathymetric relief, renewed subduction of normal oceanic crust in
167 the window of major fluid release and related volcanic activity resume the supply of detrital material to
168 the forearc basin. Interestingly, Andjić et al. (2018a) have identified delays between the onset/end of
169 forearc uplift and onset/end of volcanic activity in past collision episodes of oceanic plateau in Costa
170 Rica (middle Campanian and late Paleocene). Here, shallow-water carbonates (i.e., middle Campanian
171 El Viejo and late Paleocene Barra Honda formations; Figure 1b) deposited in response to forearc uplift
172 formed earlier than pelagic sedimentation (i.e., Piedras Blancas and Buenavista formations) resulting
173 from the cessation of volcanic arc activity: this may be the consequence of the colliding object
174 interacting first with shallow levels of the upper plate before being subducted to greater depths and
175 modifying dehydration processes in the mantle wedge (Figure 2). In contrast, the demise of shallow-
176 water carbonate factories intervened earlier than the termination of pelagic sedimentation: this may
177 result from the tail of the colliding object interacting with the mantle wedge later than it was the case
178 with the shallow upper plate (Figure 2d). Because it occurred near the Paleocene–Eocene boundary, the
179 demise of the Barra Honda shoal may not be solely attributed to local factors (e.g., forearc tectonics
180 and/or volcanoclastic input) and calls for a test of a causal link with the PETM.

181

182 **2. The Barra Honda Formation: previous work**

183

184 The Barra Honda carbonate shoal crops out in the Tempisque and Nicoya areas as erosional remnants
185 in karstified hills representing anticlines, covering today less than 60 km² (Denyer et al., 2014a), but
186 originally had a surface of >900 km² (Baumgartner-Mora & Baumgartner, 2016; Figure 3a). It was
187 defined as a formation by Dengo (1962). Mora (1981) described two subunits in the Cerro Barra Honda
188 area: a lower, poorly stratified, massive white limestone composed of algal boundstones and some
189 peloid wackestones, largely composed of micrite, and an upper stratified unit of peloidal packstones
190 and oolitic grainstones. Geological mapping (Rivier, 1983; Jaccard et al., 2001; Flores et al., 2003a,
191 2003b; compilation by Denyer et al., 2014b) shows that the formation rests unconformably on Upper
192 Cretaceous to Paleocene deep-water formations, with a highly diachronous erosional surface (Figure 4)
193 that was subaerial or paralic as suggested in the northernmost outcrops (Cerro Espiritu Santo), where
194 bored limestone clasts are set in an altered matrix of Upper Cretaceous Sabana Grande Fm. (Di Marco
195 et al., 1995; Jaccard & Münster, 2001; Jaccard et al., 2001). In the north transgression/progradation of
196 the upper Barra Honda over the altered Upper Cretaceous surface starts with lenses of cross-laminated
197 oolitic packstones and grainstones containing *Neodiscocyclina grimsdalei*, thick-shelled *Ranikothalia*
198 *catenula antillea* and *R. c. tobleri*, as well as large melobesian rhodoids encrusted by *Polystrata alba*,
199 forming bafflestones. These rather high energy, near-shore facies are overlain by calm-water, neritic
200 wackestones rich in *Distichoplax biserialis*, and thin-shelled *Ranikothalia*, such as *R. catenula catenula*

201 and *R. c. soldadensis* attesting for a late Paleocene age (Baumgartner-Mora & Baumgartner, 2016).
202 Calvo and Bolz (1991) recognized a late Paleocene–early Eocene age of the Espiritu Santo limestones
203 but did not relate them with the Barra Honda Fm.

204

205 In outcrops to the southeast (Pochote; Figure 3a), Jaccard et al. (2001) described a sequence with
206 abundant reworked pelagic limestone clasts, certainly reworked from the Piedras Blancas Fm. according
207 to the presence of the late Campanian–Maastrichtian *Globotruncana ventricosa*, included in an open-
208 marine micritic matrix containing the upper Paleocene *Morozovella velascoensis* and
209 *Pseudohastigerina* sp. Here the Barra Honda encroaches with a sharp, but apparently conformable
210 contact over the sandy forearc turbidites of the Paleocene Curú Fm. Up-section, shallow-water clasts
211 increase and a typical, massive Barra Honda facies with abundant squamariacean *Polystrata alba* follow
212 towards the top. Here, the onset of Barra Honda takes place in an offshore marine, foreslope
213 paleoenvironment without a major erosional hiatus at its base. In the lower part, Upper Cretaceous
214 lithoclasts were reworked from the substrate cropping out up-slope, while intraformational poorly
215 lithified shallow-water clasts dominate in the upper part of the section. Aguilar and Denyer (2001)
216 reported coral patch reefs from the eastern outcrops of Barra Honda, near Puerto Nispero (Figure 3a).
217 Chesnel et al. (2024) revisited the Puerto Nispero outcrops and described typical Barra Honda facies
218 interbedded with a coral patch reef attributed by them to a Maastrichtian age, based on the presence of
219 *Nerinea* and the coral genus *Marcelohelia* sp. These carbonates around Puerto Nispero, along the East
220 bank of the lower Tempisque estuary (Figure 3a) were previously mapped as Barra Honda Fm. (Denyer
221 et al., 2014b), and represent undoubtedly the lowest (and oldest) part of this formation, resting
222 unconformably on hemipelagic lime- and claystone attributed to the Campanian-Maastrichtian Piedras
223 Blancas Fm. (Denyer et al., 2014b).

224

225 Unfortunately, Chesnel et al. (2024) defined a new “Puerto Nispero Fm.”, which includes both the
226 deformed hemipelagic “claystone” and the unconformably overlying shallow carbonates, defining
227 rather a Maastrichtian “chronozone” than a formation in the sense of the International Code of
228 Stratigraphy (Murphy & Salvador, 1999). However, the illustrated, poorly preserved, planktonic
229 foraminifera of the “claystone” (*Rugoglobigerina rugosa* and *Globotruncanella* sp.) range from middle
230 Campanian to Maastrichtian (Huber et al., 2016; Petrizzo et al., 2020), which fits the age range of the
231 Piedras Blancas Fm.

232

233 Baumgartner-Mora and Baumgartner (2016) produced a refined model that shows an asymmetric
234 carbonate shoal fringing an uplifted and tilted area of the forearc. Based on the available biostratigraphic
235 data, these authors postulated a late Paleocene rapid south to north onlap of the Barra Honda shoal. The
236 probably uppermost Cretaceous very shallow coral-bearing Barra Honda facies described by Chesnel
237 et al. (2024) encroached on a local, probably subaerial paleo-high where the substrate was eroded down
238 to the Campanian-Maastrichtian pelagic sediments of the Piedras Blancas Fm. The Puerto Nispero
239 outcrops are located in the core of a roughly North–South-oriented anticline (Denyer et al., 2014b),
240 which is flanked on both sides by higher Barra Honda facies. Although the stratigraphic continuity
241 towards higher Barra Honda facies cannot be observed and fossils attesting for early Paleocene ages are
242 lacking, a stratigraphic continuity can be assumed. Hence, uplift occurred first in the southwest followed
243 by subsidence, while uplift moved to the northeast followed by subsidence during the late Paleocene
244 when a shallow, restricted lagoon produced the chloralgal carbonate mud of the upper Barra Honda. Its
245 high production resulted in sediment export towards deeper, offshore areas (e.g., Pochote), where the
246 progradation of the shallow environments finally produced an oolitic rim.

247

248 In the Cerro Calera, facing the Nicoya town (Figure 3a), Barra Honda rests with a tectonic contact on
249 both the underlying Curú Fm. and the lower Eocene Zapotal Member (Mb.) of the Descartes Fm.
250 (Denyer et al., 2014a, 2014b). The latter was originally mapped as Upper Cretaceous Sabana Grande
251 Fm. (Flores et al., 2003a), because it contains cherty facies (here considered as part of the Buenavista

252 Fm.) that resemble those of the Zapotal Mb. We have modified the geological map (Figure 3b)
253 according to our observations in the Teresita quarry area, and a radiolarian sample described from this
254 unit by Bandini et al. (2008) is reevaluated in this study as of early Ypresian (early Eocene) age.

255

256 **3. Materials and methods**

257

258 *3.1. Field work and sampling*

259

260 Two upper Paleocene–lower Eocene sections were measured and sampled in the Tajo Santa Teresita
261 (here called “Teresita quarry”), located 4.5 km east of the town of Nicoya (Costa Rica; Figure 3b). The
262 quarry section (code TTQ; 10°08'36.66"N /85°24'47.16"W) is about 109 m thick, whereas the road
263 section (code TTR; 10°08'24.78"N/85°24'45.60"W) is about 3 m thick. The 0-meter mark in these
264 stratigraphic logs has been placed at the boundary between the Barra Honda Fm. and the Buenavista
265 Fm.

266

267 *3.2. Micropaleontological analysis*

268

269 Thin sections from 28 samples were examined with an optical microscope to characterize the facies and
270 microfossils. Polished thin sections were scanned with an Olympus VS110 slide scanner. A motor-
271 driven turntable can take several hundred overlapping images to produce an image of about 12'000 x
272 26'000 pixels with a 4x lens, resulting in a resolution of about 622 pixels/mm (pixel size 1.6 μ m). This
273 resolution is sufficient to allow detailed analysis of microfossils across an entire thin section.

274

275 For a coherent biochronologic interpretation of new and existing (Appendix A) data on planktonic
276 foraminifera we use the zonation summarized in Olsson et al. (1999), Pearson et al. (2006), Wade et al.
277 (2011), and Huber et al., (2016), and its calibration to absolute time by Speijer et al. (2020), in which
278 the Paleocene–Eocene boundary is defined by the negative $\delta^{13}\text{C}$ -shift of the PETM (Aubry et al., 2007).
279 For a re-evaluation of a radiolarian assemblage published in Bandini et al. (2008), we use the zonation
280 of Jackett et al. (2008).

281

282 *3.3. Optical cathodoluminescence*

283

284 40 μ m polished thin sections were used for cathodoluminescence optical analyses (CL). CL images
285 were obtained using an OPEA electron gun adapted to the vacuum chamber of a CTTL, Technosyn
286 8200 MkII, mounted on an Olympus optical microscope with a mobile tube and an object stage fixed
287 in height. The OPEA was operated at 15-20 kV and 0.4-0.5 mA with an unfocused cold cathode electron
288 beam under an air atmosphere of 0.2 torr.

289

290 *3.4. CA-ID-TIMS on zircon*

291

292 Zircon was separated from the sediment in the laboratories of the University of Lausanne.
293 Approximately 1 to 2 kg of the ash-rich layer TTR5 was crushed and then decarbonated for three days
294 using 35% HCl. After several washings, the sample was treated with hydrogen peroxide (H_2O_2) for 5
295 days to disperse the clays. The dispersion of the clays was finalized by heating the hydrogen peroxide.
296 The sample was then treated for three weeks with 40 % hydrofluoric acid (HF) to dissolve minerals
297 such as quartz or feldspar.

298

299 U–Pb chemical abrasion isotope dilution thermal ionization mass spectrometry (CA-ID-TIMS) was
300 used to date the zircon grains at the University of Geneva. Individual zircon crystals free of visible
301 inclusions and cracks were hand-picked using a binocular microscope at a magnification of 20x to 40x.
302 Individual zircons were washed in 3 ml Savillex beakers in an ultrasonic bath 4 times using 7N HNO_3 .

303 The zircons were then transferred into individual 200 μL Savillex microcapsules, along with 1-2 drops
304 of HF_{conc} and 1-2 drops of a mixed ^{202}Pb - ^{205}Pb - ^{233}U - ^{235}U tracer solution (ET2535, Condon et al., 2015;
305 McLean et al., 2015), and dissolved at 210 $^{\circ}\text{C}$ in a Parr bomb for 48 hours, to ensure complete
306 dissolution. After dissolution, samples were dried down on a hotplate at 120 $^{\circ}\text{C}$, converted to chloride
307 form by addition of 6N HCl and placed back in the Parr bomb over-night. Finally, the sample is again
308 dried and re-dissolved in 3N HCl, and then U and Pb were separated using a single column anion
309 exchange chemistry. U and Pb were loaded on outgassed, zone-refined, single Re filaments with a silica-
310 gel/phosphoric acid emitter solution (Gerstenberger & Haase, 1997).

311
312 Pb was measured in dynamic mode using a Daly detector, while U was measured as an oxide in static
313 mode using Faraday detectors coupled to 1012 Ω resistor amplifiers. The electronic baselines and
314 amplifier calibration was performed on a weekly basis, prior to standard and unknown sample analyses.
315 Measured isotopic ratios were corrected for interferences of $^{238}\text{U}^{18}\text{O}^{16}\text{O}$ on $^{235}\text{U}^{16}\text{O}_2$ using a $^{18}\text{O}/^{16}\text{O}$
316 composition of 0.00205, based on repeated measurements of the U500 standard. Mass fractionation of
317 Pb is calculated and corrected using a $^{202}\text{Pb}/^{205}\text{Pb}$ ratio of $0.99923913 \pm 0.00026555$ (1σ) (Condon et
318 al., 2015). For all U analyses, U mass fractionation is corrected using a $^{233}\text{U}/^{235}\text{U}$ ratio of $0.995062 \pm$
319 0.000108 (2σ) and a $^{238}\text{U}/^{235}\text{U}$ ratio of 137.818 ± 0.045 (2σ) (Hiess et al., 2012; Condon et al., 2015).
320 The common Pb in zircon is considered laboratory blank, and is corrected using the isotopic
321 composition $^{206}\text{Pb}/^{204}\text{Pb}$ of 17.43 ± 0.71 , a $^{207}\text{Pb}/^{204}\text{Pb}$ of 14.73 ± 0.38 and a $^{208}\text{Pb}/^{204}\text{Pb}$ of 35.58 ± 1.04 .
322 All U-Pb dates are corrected for initial ^{230}Th disequilibrium, assuming a Th/U ratio of the source magma
323 of 3.5 ± 1 . During the period of data acquisition, the ET 100 solution was repeatedly analyzed and
324 yielded a weighted mean of 100.176 ± 0.006 Ma (MSWD = 2; n = 22), matching the consensus value
325 of 100.173 ± 0.003 Ma (Schaltegger et al., 2021).

326
327 All data were processed using the Tripoli, Redux U-Pb, YourLab and Isoplot software/excel packages
328 (Ludwig, 1991; McLean et al., 2011; Schmitz & Schoene, 2007; Bowring et al., 2012). Weighted mean
329 U-Pb age uncertainties are reported at the 2σ level in the format $A \pm X/Y/Z$, where A is the weighted
330 mean age, X is analytical uncertainty, Y is analytical and tracer uncertainty combined, and Z is
331 analytical, tracer, and decay constant uncertainties combined (Schoene et al., 2006). Lower intercept
332 ages are calculated for samples with assumed inherited components and discordance. The results are
333 presented in Table S1 (Supporting Information S1).

334 3.5. X-Ray diffraction on bulk rocks

335
336 Bulk-rock mineralogy of 29 samples has been analyzed using an X-TRA Thermo-Arl SCINTAG 2000
337 diffractometer, following the procedures of Kübler (1983) and Adatte et al. (1996). The whole-rock
338 mineralogy was determined by a semi-quantitative method, using XRD peak intensities of the main
339 minerals in comparison with external standards (Klug & Alexander, 1974; Kübler, 1983; Adatte et al.,
340 1996). The precision is 5 wt% for grain minerals and 5 to 10 wt% for phyllosilicates. The results are
341 presented in Table S2 (Supporting Information S1).

342 3.6. Stable isotope compositions

343
344 Oxygen and carbon isotope analyses (48 samples) were made in the stable isotope laboratory of the
345 University of Lausanne with a Gas-Bench II interfaced with a Thermo Fisher Scientific DeltaPlus XL
346 isotope ratio mass spectrometer following a method described in Spötl & Vennemann (2003). The stable
347 carbon and oxygen isotope ratios are expressed in delta notation as per mil (‰) relative to the Vienna
348 Pee Dee Belemnite (VPDB) international reference standard. Multiple analyses of an in-house standard
349 (Carrara marble, calibrated to international carbonate standards), were run parallel with the samples to
350 correct raw isotopic values. The analytical precision of the method is better than ± 0.1 ‰ (1σ) for both
351 C- and O-isotope compositions. The results are presented in Table S3 (Supporting Information S1).

354
355
356
357
358
359
360
361
362
363
364
365
366
367
368
369
370
371
372
373
374
375
376
377
378
379
380
381
382
383
384
385
386
387
388
389
390
391
392
393
394
395
396
397
398
399
400
401
402
403
404

4. Results

4.1. Log description

The lower part of the quarry section consists of 64 m of shallow-water limestones with some levels rich in cherts (at -53 m, -50 m and -0.2 m below the top of the Barra Honda Fm.; Figure 5). The upper part of the quarry section is characterized by marls and detrital deposits. The first 7 meters above the Barra Honda Fm. are characterized by a high proportion of marls and clays with some cherts, sandy beds, and rare centimetric ash layers (Buenavista Fm.). The uppermost part of the quarry section corresponds to turbiditic deposits with some marl intercalations (Zapotal Mb.). The shorter road section presents the same lithological association as the quarry section. The first meter of the road section is characterized by massive shallow-water limestones of the Barra Honda Fm. with the presence of cherts a few tens of centimeters below its top. The upper part of the road section is dominated by clayey deposits and cherts, with scarce centimetric ash layers (at 0.05 m, 0.5 m, and 1 m) and sandy beds, which is similar to the facies association deposited on top of the Barra Honda Fm. in the quarry section.

From a facies perspective, the massive shallow-water limestones of both sections are characterized by red algal packstones and wackestones. Most of these limestones contain *Polystrata alba*, *Melobesia*, larger benthic foraminifera, miliolids, planktonic foraminifera and some siliceous sponges. Pack- to wackestone microfacies and *Polystrata alba* (Pfender, 1936; Denizot, 1968) are very common in most of the upper Barra Honda rocks. This squamariacean red alga encrusted rhodoids and other firm substrates. It is typical of algal platforms of the Upper Cretaceous and Paleocene, although its range extends from the Barremian to the Eocene (Massieux & Denizot, 1964; Pratulon, 1966; Baumgartner-Mora & Baumgartner, 2016). The upper part of the quarry and road sections is characterized by alternating clayey and sandy deposits, with low carbonate proportions. Thin sections show wackestone to mudstone microfacies including mainly planktonic foraminifera (such as *Morozovella*), sponge spicules, radiolarians, and debris of red algae. These deposits are characteristic of an open sea environment receiving a significant detrital input.

4.2. Biostratigraphic ages

Sample TTQ650 is a pelagic limestone rich in planktonic foraminifera (Figure 6) from the Buenavista Fm., that was recovered 6.5 m above the top of the Barra Honda limestone (quarry section; Figure 5). It yielded *Acarinina* cf. *quetra* (top E3-E6 Zones), *Morozovella subbotinae* (P5-E5 Zones), *Morozovella gracilis* (P5-E5 Zones), *Planorotalites pseudoscitula* (P5-E7 Zones), *Morozovella aequa* (P4c-E5 Zones), *Morozovella* cf. *formosa*, *Morozovella* cf. *lensiformis*, and *Acarinina angulosa* (P5-E7 Zones). The concurrent range of these taxa is from top E3 to E5 Zones (early to middle Ypresian age).

In an earlier study (Bandini et al., 2008), we described a radiolarian fauna of sample 01-18-01-02 from the Teresita quarry area in the transition from the Buenavista Fm. to the Zapotal Mb. of the Descartes Fm. The sample was collected about 30 m east of the eastern rim (quarry limits in 2020) of the Teresita quarry at 10° 8'38.29"N, 85°24'49.06"E (Figure 3b). Bandini et al. (2008) concluded on a late Thanetian to Ypresian age of this sample. Here we slightly revise the taxonomy and the age ranges of the taxa encountered, based on the UA-zonation of Jackett et al. (2008). The sample contains *Lychnocanium carinatum* (UA 11-12), *Podocyrtis (Podocyrtis) papalis* (UA 11-22), *Phormocyrtis striata exquisite* (UA 3-20), *Stylotrochus nititus* (UA 5-22), *Circodiscus circularis* (UA 5-22), *Phormocyrtis turgida* (UA 11-22), *Calocyclas hispida* (UA 11-22), *Stylosphaera coronata coronata* (UA 1-22), and *Buryella tetradica* (UA 2-20). Of this association several species are not older than UAZ 11 (base of the Eocene) and *Lychnocanium carinatum* is restricted to UA 11-12 in Jackett et al. (2008). These two Unitary

405 Associations correlate with the planktonic foraminiferal zones (see Pearson et al., 2006) P5 top half
406 (=E1-E2 Zones) and P6a-b (=E3-E4 Zones), indicating an early Ypresian age. This age overlaps with
407 the age range of planktonic foraminifera from the new sample TTQ650, collectively suggesting that the
408 Buenavista Fm. is restricted to the early to middle Ypresian in the Teresita quarry.

409

410 *4.3. U–Pb zircon CA-ID-TIMS age*

411

412 Ash-rich layer TTR5 was sampled 5 cm above the limit between massive limestones of the Barra Honda
413 Fm. and overlying clayey beds of the Buenavista Fm. Five single-grain zircon analyses were undertaken
414 on sample TTR5, all of which are concordant within analytical and decay constant uncertainties (Figure
415 7). Four out of five analyses cluster between 56 and 57 Ma, whereas one analysis yielded a distinctly
416 older age (62.4 Ma) than that of all other analyses. The younger cluster of $^{206}\text{Pb}/^{238}\text{U}$ dates yield a
417 weighted mean date of $56.30 \text{ Ma} \pm 0.11/0.12/0.13 \text{ Ma}$ (2σ , $n = 3$, $\text{MSWD} = 2.2$), which approximates
418 the depositional age of the ash-rich layer TTR5.

419

420 *4.4. Bulk-rock mineralogy*

421

422 The mineralogy of the quarry and road sections is mainly composed of calcite, quartz, and
423 phyllosilicates, with minor amounts of plagioclase and alkali feldspar, and punctual presence of
424 dolomite, ankerite, and goethite (Figure 5). The unquantified fraction represents generally less than 3
425 wt% and may correspond to poorly crystallized clays, Fe-oxides, Fe-hydroxides, zeolites and organic
426 matter. For each section, two parts can be distinguished based on mineralogical contents.

427

428 The lower part of the quarry and road sections consists of 81 to 98 wt% calcite and very low proportions
429 of quartz and phyllosilicates. This part coincides with massive limestones of the Barra Honda Fm. (–65
430 m to 0 m in the quarry section, –0.7 m to 0 m in the road section).

431

432 The upper part of the quarry and road sections consists of variable proportions of phyllosilicates (0–83
433 wt%), quartz (1 to 94 wt%), and calcite (0 to 63 wt%), which coincide with ash-rich beds, cherts, and
434 clayey deposits (0 m to 44 m in the quarry section, 0 m to 2.3 m in the road section). This mineralogical
435 variability reflects the lithological heterogeneity of the Buenavista Fm. and Zapotal Mb.: (i) cherts at
436 0.75 m/12 m in the quarry section and at 0.75 m/1.75 m in the road section present high amounts (> 70
437 wt%) of quartz; (ii) ash-rich beds at 0.05 m/0.5 m/1 m in the road section have high proportions (63 to
438 83 wt%) of phyllosilicates; (iii) marls throughout the quarry section and at one level of the road section
439 show a mix of siliciclastic material (6 to 30 wt% phyllosilicates, 1 to 40 wt% quartz, 0 to 7.5 wt% alkali
440 feldspar, and 0.5 to 9 wt% plagioclase) and calcite (35 to 63 wt%).

441

442 *4.5. Stable isotope geochemistry*

443

444 *4.5.1. $\delta^{13}\text{C}_{\text{carb}}$*

445

446 $\delta^{13}\text{C}_{\text{carb}}$ values have a range between –0.8 ‰ and 4.3‰ in the quarry section (Figure 5). In the lower
447 part of the section (middle to upper Thanetian Barra Honda Fm.), most values are around 2.8 ‰ except
448 for two positive shifts towards 4.3 ‰ at –50 m and 4.0 ‰ at –0.6 m. A shift of –3.3 ‰ occurs across
449 the boundary between the Barra Honda Fm. and the Buenavista Fm. This is followed by a positive shift
450 to 2.4 ‰ at 0.8 m and a second negative shift to –0.3 ‰ at 2 m, at the base of the lower Ypresian
451 Buenavista Fm. $\delta^{13}\text{C}_{\text{carb}}$ values increase from –0.3 ‰ at 2 m (Buenavista Fm.) to 2.4 ‰ at 14 m (Zapotal
452 Mb.), after which they steadily decrease towards 1.3 ‰ at 40 m.

453

454 $\delta^{13}\text{C}_{\text{carb}}$ values vary between –3.9 ‰ and 2.2 ‰ in the road section. The $\delta^{13}\text{C}_{\text{carb}}$ values are homogeneous
455 at around 1.8 ‰ in the uppermost Barra Honda Fm. A significant decrease to –3.9 ‰ coincides with

456 the base of the Buenavista Fm. The very low carbonate contents (<2 wt%) of the Buenavista Fm. from
457 0.5 m to 2.3 m precludes the analysis of carbon isotopes.

458

459 4.5.2. $\delta^{18}O_{carb}$

460

461 $\delta^{18}O_{carb}$ values range from -7.2 to -1.3 ‰ in the quarry section and from -8.3 to -1.7 ‰ in the road
462 section (Figure 5). In both sections, a negative shift occurs around the boundary between the Barra
463 Honda Fm. and the Buenavista Fm., which is 2.5 ‰ in the quarry section and 6.6 ‰ in the road section.
464 In the quarry section, the $\delta^{18}O_{carb}$ record shows an overall decreasing trend above the formational
465 boundary; values decrease from -4.9 ‰ at 2 m to -7.2 ‰ at 40 m, except for two positive excursions
466 towards -2.4 ‰ at 4 m and towards -4.3 ‰ at 25 m.

467

468 5. Discussion

469

470 5.1. Barra Honda–Buenavista boundary: a record of the PETM?

471

472 The sharp lithological boundary between the Barra Honda and Buenavista formations has been
473 previously interpreted as the demise of the Barra Honda carbonate shoal (Baumgartner-Mora &
474 Baumgartner, 2016). The latter authors argued that the rapid demise of the carbonate shoal occurred
475 through a combination of factors, which are (i) a relative sea level rise due to tectonic subsidence and
476 an eustatic component, (ii) and a paleoclimatic change around the Paleocene–Eocene boundary
477 resulting in intensified weathering, river runoff and eutrophication of the forearc basin by detrital input
478 and dissolved organic matter. To discuss how these factors combined to cause the demise of the Barra
479 Honda carbonate shoal, we first use our new data from the Teresita quarry to determine whether the
480 timing of termination of carbonate shoal sedimentation was coeval with the PETM.

481

482 A large negative excursion of 3 to 5 ‰ in $\delta^{13}C_{carb}$ values in both Teresita quarry sections coincides with
483 a prominent decrease in average calcite contents, from 90 % calcite in massive limestones of the
484 uppermost Barra Honda Fm. to about 40 % calcite in overlying clayey layers of the lowermost
485 Buenavista Fm. (Figure 5). Despite being analyzed in clayey beds with similar carbonate contents
486 (estimated $CaCO_3$ yield = 28 to 39 %) in the quarry section, $\delta^{13}C_{carb}$ values at the base of the Buenavista
487 Fm. span a wide range (from -0.8 to 2.5 ‰), which makes it unlikely that the change in calcium
488 carbonate contents and lithology across the Barra Honda–Buenavista boundary had a significant effect
489 on $\delta^{13}C_{carb}$ values. Instead, the timing of the combined lithological-mineralogical-isotopic change at the
490 Barra Honda–Buenavista boundary is consistent with the PETM, which is supported by new U–Pb
491 zircon CA-ID-TIMS age data, as well as new and existing biostratigraphic data. The fact that our new
492 zircon age (56.30 ± 0.13 Ma) of the lowermost Buenavista Fm. is 0.1 to 0.3 Ma older than the currently
493 established Paleocene–Eocene boundary age (56 Ma) may result from averaging the age of only three
494 zircon grains, among which one older grain (56.5 ± 0.3 Ma) is pooled together with two younger zircon
495 grains (56.2 ± 0.1 Ma and 56.1 ± 0.3 Ma).

496

497 The synchronicity of the Barra Honda–Buenavista boundary with the PETM can be further examined
498 by comparing our new $\delta^{13}C_{carb}$ curve of the quarry section to the most recent global $\delta^{13}C$ curve of Speijer
499 et al. (2020). Although the nature and rate of sedimentation differ among the Barra Honda, Buenavista,
500 and Descartes formations, the overall shape of our new $\delta^{13}C_{carb}$ curve of the quarry section approximates
501 the global Thanetian–Ypresian $\delta^{13}C$ curve (Figure 8), with the following key similarities: (i) two
502 positive carbon isotope excursions occur in the Thanetian; (ii) a negative carbon isotope excursion (>2.5
503 ‰) characterizes the base of the Ypresian and is related to the PETM; (iii) Ypresian $\delta^{13}C$ levels are
504 about 1.5 ‰ lower after the PETM negative carbon isotope excursion when compared to pre-PETM
505 levels in the Thanetian.

506

507 *5.2. Step-wise demise of Barra Honda carbonate shoal*

508

509 The onset of shallow-water carbonate sedimentation in the Barra Honda shoal was favored by the
510 combination of moderate tectonic subsidence and volcanic quiescence (Figure 9a). Tectonic subsidence
511 followed a short-lived episode of km-scale forearc uplift, possibly related to the subduction of
512 bathymetric features (Andjić et al., 2018a; Figure 2b). Once they entered deeper parts of the subduction
513 interface, the bathymetric features caused cessation of volcanic activity within the Barra Honda area.
514 The proximal forearc basin floor was shortly exposed to subaerial environments before initial moderate
515 subsidence to shallow waters that favored the accumulation of the Barra Honda carbonate shoal (Jaccard
516 et al., 2001; Baumgartner-Mora & Baumgartner, 2016; Figure 2c). Volcanic quiescence resulted in the
517 reduction of the input of proximal coarse-grained volcanoclastic sediments compared to the underlying
518 deep-water forearc formations. Only distal ash particles carried from distant volcanic sources made
519 their way to the upper Barra Honda shoal, as suggested by discrete contents of phyllosilicates in the
520 massive limestones (Figure 5; Baumgartner-Mora & Baumgartner, 2016). The lifespan of about 5 Ma
521 and the thickness (350 m) of the upper Barra Honda shoal implies an average subsidence rate of the
522 forearc basin of 70 m/Ma during the late Paleocene (61 to 56 Ma). This subsidence rate is comparable
523 to that of long-lived (>10 Ma) carbonate platforms on passive margins (36 to 150 m/Ma; Immenhauser,
524 2021). This, however, raises the question as to why the shallow-water carbonate sedimentation of the
525 upper Barra Honda shoal stopped at the Paleocene–Eocene boundary? In the following sections, we
526 envisage a sequence of events that eventually led to the demise of the upper Barra Honda carbonate
527 shoal during the earliest Ypresian.

528

529 *5.2.1. Step 1 (56 Ma): Environmental effects of the PETM*

530

531 The PETM may have affected the Barra Honda carbonate shoal in at least two ways. Global ocean
532 acidification due to increased CO₂ levels resulted in reduced rates of accumulation and preservation of
533 carbonate sediments in shelf areas (Bralower et al., 2018). In addition, the rise of sea surface
534 temperatures (about 5 °C; e.g., McInerney & Wing, 2011) during the PETM reached levels that were
535 probably beyond the tolerance range of benthic foraminifera, calcareous algae, and coral patch reefs of
536 the Barra Honda carbonate shoal (e.g., Scheibner & Speijer, 2008). Moreover, increased precipitation
537 at the onset of the PETM may have caused an increased discharge of fluvial sedimentary organic matter
538 to shelf areas, favoring the proliferation of non-calcifying organisms such as dinoflagellates and bacteria
539 (Sluijs et al., 2006; Kopp et al., 2009; Handley et al., 2012; Aze et al., 2014; Carmichael et al., 2017).
540 Input of nutrients led to higher surface-water productivity and anoxic to low oxygen levels in bottom
541 shelf waters (Sluijs et al., 2006, 2008). There is currently no quantitative data available from the
542 Tempisque Forearc Basin to constrain whether an absolute increase in abundance and size of detrital
543 grains occurred during the earliest Eocene. At the outcrop scale, basinal sections of the western Nicoya
544 Peninsula and northern Santa Elena Peninsula (Figure 1b) show that there was no increase in volcanic
545 activity inboard the Nicoya Peninsula around the Paleocene–Eocene boundary: pelagic sedimentation
546 of the Buenavista Fm. dominated that interval (Figure 4) and only airborne ash was brought into the
547 forearc basin from outboard volcanoes (Figure 2d). Rather, the onset of coarse detrital sedimentation of
548 the Zapotal Mb. took place 3 to 4 Ma after the demise of the Barra Honda carbonate shoal, in response
549 to renewed volcanic activity inboard the Nicoya Peninsula (Figures 2e and 9b). Nevertheless, the
550 relative increase of the phyllosilicates/calcite ratio (from 1/18 to 1/2) and feldspars/calcite ratio (from
551 1/200 to 1/20) in the Teresita quarry is larger than the decrease by 50 % of carbonate proportions across
552 the Barra Honda–Buenavista boundary (Figure 5), which may indicate that mud-sized clastic input and
553 turbidity increased on the shelf during the earliest Ypresian, possibly in response to enhanced river
554 discharge. The resulting reduced light intensity in surface waters would have led to a much shallower
555 photic zone, contributing to the demise of the benthic communities relying on oligotrophic waters. This
556 hypothesis remains to be tested in basinal sections of the Buenavista Fm. (e.g., Santa Elena area) by
557 establishing whether a change in mineralogical contents coincided with the PETM.

558

559 Moreover, the presence of cherts in the Buenavista Fm. supports the view of increased opal production
560 and burial to balance elevated weathering flux of silica (e.g., Penman et al., 2019). The latter possibly
561 resulted from enhanced continental weathering and runoff in a warmer climate with increased
562 seasonality of precipitation (McInerney & Wing, 2011). Excess silica that could not be incorporated in
563 clay-rich layers of the Buenavista Fm. may have precipitated as opal-rich layers that later formed cherts
564 (e.g., Muttoni & Kent, 2007). The proportion of nutrients brought by upwelling currents vs. terrestrial
565 influx remains unconstrained in this case, although climate–carbon cycle models with high-CO₂ levels
566 predict that a weakening of the trade winds would lead to reduced Ekman-induced upwelling and
567 nutrient availability in the equatorial Pacific (Winguth et al., 2012; Wade et al., 2020). However, it
568 remains possible that upwelled water, characterized by low $\delta^{13}\text{C}$ values and high nutrient content (e.g.,
569 Watanabe et al., 2017), influenced the isotopic compositions of the Buenavista Formation and the
570 production of biogenic silica.

571

572 *5.2.2. Step 2 (56–55 Ma): Onset of accelerated tectonic subsidence and eustatic sea level rise*

573

574 Extreme environmental conditions linked to the PETM were short-lived (about 0.2 Ma; Murphy et al.,
575 2010; Zeebe & Lourens, 2019), after which the production of carbonates resumed in both deep-water
576 and shallow-water settings globally (e.g., Zachos et al., 2005; Scheibner & Speijer, 2008). We speculate
577 that the short duration of the hyperthermal event would have made it possible for the Barra Honda
578 carbonate shoal to recover during the early Ypresian and to resume shallow-water carbonate
579 sedimentation, as suggested by the deposition of early to middle Eocene shallow-water carbonates in
580 the most proximal parts of the forearc basin (Laguna El Jicote; Jaccard et al., 2001; Figures 3a and 4).
581 The fact that this did not occur may be primarily attributable to accelerated forearc subsidence that must
582 have taken place by 55 Ma, not allowing renewed formation and deposition of carbonates in shallow
583 shelf environments (Figure 9b). The fate of uplifted highs in forearc areas affected by subduction of
584 bathymetric features is clear: once the impinging bathymetric feature has been subducted, uplifted
585 forearc areas return to their pre-collisional morphology within 3 Ma at rates similar to those of the uplift
586 episode (e.g., Corrigan et al., 1990; Cloos, 1993; Meffre & Crawford, 2001; Andjić et al., 2018a; Figure
587 2). In the case of the Tempisque Forearc Basin, the pre-collisional depth of the forearc basin floor (=
588 Paleocene Curú Fm.) is estimated to be about 3000 m based on benthic foraminifera (Struss et al., 2008).
589 Assuming that the proximal forearc basin returned to a water depth of 3000 m within 3 Ma after the
590 PETM, a subsidence rate of 1000 m/Ma would have brought the Barra Honda to a depth of 1000 m by
591 55 Ma, largely exceeding the rate of sediment supply of any carbonate shoal. In contrast, moderate
592 subsidence (70 m/Ma) combined with an early Ypresian 3rd-order eustatic sea level rise (30 m by 55
593 Ma; Speijer et al., 2020; Figure 8) may not explain the absence of post-PETM recovery of the Barra
594 Honda shoal, because a relative sea level rise of similar magnitude already occurred from 60 to 58 Ma
595 without preventing deposition of shallow-water carbonates.

596

597 **6. Conclusions**

598

599 Our work shows a sharp transition from massive shallow-water limestones of the upper Barra Honda
600 Fm. to marl-chert alternations of the Buenavista Fm. in the Tempisque Forearc Basin at the Paleocene–
601 Eocene boundary (56 Ma). The lithological and mineralogical change at the Barra Honda–Buenavista
602 boundary is accompanied by a negative shift in carbon isotope ($\delta^{13}\text{C}_{\text{carb}}$) values of 3 to 5 ‰ and an
603 increased detrital input. We postulate that the combination of two events caused the demise of the Barra
604 Honda carbonate shoal during the earliest Eocene. First, the PETM led to a significant disturbance of
605 the local oceanographic conditions of the forearc area: during the earliest Ypresian, seawater warming,
606 acidification, eutrophication, and increased river runoff as well as likely upwelling may have led to a
607 shift to siliceous sedimentation in the Buenavista Formation. These environmental changes were highly
608 detrimental to the shallow benthic communities that had formed the upper Barra Honda carbonate shoal

609 during the Thanetian. Secondly, accelerated subsidence of the Tempisque Forearc Basin closely
610 followed the short-lived PETM event. Shallow shelf areas that were initially favorable to the
611 establishment of the Barra Honda carbonate shoal gave way to deep-water basinal environments by 55
612 Ma, which did not allow a recovery of the Barra Honda carbonate shoal. After the PETM, the warm
613 climate of the early Eocene was not a limiting factor to the growth of carbonate shoals in Costa Rica
614 and Nicaragua (e.g., Baumgartner-Mora & Baumgartner, 2016; Andjić et al., 2018b). Locally, shallow-
615 water carbonate sedimentation occurred on tectonic highs that provided a shelter from river discharges
616 carrying volcanoclastic sediments from active volcanoes.

617

618 **Acknowledgements**

619

620 We are thankful to the previous owner of the Santa Teresita quarry for allowing us the access to the
621 outcrops. This study was supported by the Swiss National Science Foundation grant no. 185067 to
622 C.B.M.

623

624 **Open research**

625

626 New data generated in this study are available in the Supporting Information S1, and can also be found
627 in <https://zenodo.org/communities/geodiversity/> (detailed link to be provided).

628

629 **References**

630

631 Adatte, T., Stinnesbeck, W., & Keller, G. (1996). Lithostratigraphic and mineralogic correlations of
632 near K/T boundary clastic sediments in northeastern Mexico: implications for origin and nature of
633 deposition. *Geological Society of America Special Papers*, 307, 211–226. [https://doi.org/10.1130/0-](https://doi.org/10.1130/0-8137-2307-8.211)
634 [8137-2307-8.211](https://doi.org/10.1130/0-8137-2307-8.211)

635

636 Aguilar, T., & Denyer, P. (2001). Una nueva especie de Euphyllia (Scleractinia: Caryophylliidae) en las
637 calizas de Barra Honda (Paleógeno), Costa Rica. *Revista de Biología Tropical*, 2, 195–201.

638

639 Alvarado, G. E., Dengo, C., Martens, U., Bundschuh, J., Aguilar, T., & Bonis, S. B. (2007). Stratigraphy
640 and geologic history. In J. Bundschuh & G. E. Alvarado (Eds.), *Central America: Geology, resources,*
641 *hazards* (Vol. 1, pp. 345–394). London: Taylor & Francis. <https://doi.org/10.1201/9780203947043>

642

643 Andjić, G., Baumgartner, P. O., & Baumgartner-Mora, C. (2018a). Rapid vertical motions and
644 formation of volcanic arc gaps: Plateau collision recorded in the forearc geological evolution (Costa
645 Rica margin). *Basin Research*, 30(5), 863–894. <https://doi.org/10.1111/bre.12284>

646

647 Andjić, G., Baumgartner, P. O., & Baumgartner-Mora, C. (2019a). Collision of the Caribbean Large
648 Igneous Province with the Americas: Earliest evidence from the forearc of Costa Rica. *Geological*
649 *Society of America Bulletin*, 131(9-10), 1555–1580. <https://doi.org/10.1130/B35037.1>

650

651 Andjić, G., Baumgartner-Mora, C., & Baumgartner, P. O. (2016). An upper Paleogene shallowing-
652 upward sequence in the southern Sandino Forearc Basin (NW Costa Rica): Response to tectonic uplift.
653 *Facies*, 62, 1–35. <https://doi.org/10.1007/s10347-016-0463-y>

654

655 Andjić, G., Baumgartner-Mora C., Baumgartner P. O., & Petrizzo M. R. (2018b). Tectono-stratigraphic
656 response of the Sandino Forearc Basin (N-Costa Rica and W-Nicaragua) to episodes of rough crust and
657 oblique subduction. *The Depositional Record*, 4, 90–132. <https://doi.org/10.1002/dep2.40>

658

- 659 Andjić, G., Escuder-Viruete, J., Baumgartner-Mora, C., Baumgartner, P. O., Mitchell, S. F., Caron, M.,
660 & Caus, E. (2019b). Sedimentary record of arc-continent collision along Mesozoic SW North America
661 (Siuna Belt, Nicaragua). *Tectonics*, 38. <https://doi.org/10.1029/2019TC005741>
662
- 663 Arenillas, I., Molina, E., & Schmitz, B. (1999). Planktic foraminiferal and $\delta^{13}\text{C}$ isotopic changes across
664 the Paleocene/Eocene boundary at Possagno (Italy). *International Journal of Earth Sciences*, 88, 352–
665 364. <https://doi.org/10.1007/s005310050270>
666
- 667 Astorga, A. (1987). El Cretácico Superior y el Paleógeno de la vertiente pacífica de Nicaragua
668 meridional y Costa Rica septentrional: Origen, evolución y dinámica de las cuencas profundas
669 relacionadas al margen convergente de Centroamérica. Tesis de Licenciatura, Universidad de Costa
670 Rica, 250 p.
671
- 672 Astorga, A. (1988). Geodinámica de las cuencas del Cretácico Superior- Paleógeno de la región
673 “forearc” del Sur de Nicaragua y Norte de Costa Rica. *Revista Geológica de América Central*, 9, 1–40.
674 <https://doi.org/10.15517/rgac.v0i09.12959>
675
- 676 Aubry, M. P., Ouda, K., Dupuis, C., Berggren, W. A., Van Couvering, J. A., & Boundary
677 TMOTWGOTP (2007). The Global Standard Stratotype-section and Point (GSSP) for the base of the
678 Eocene Series in the Dababiya section (Egypt). *Episodes*, 30, 271–286.
679 <https://doi.org/10.18814/epiugs/2007/v30i4/003>
680
- 681 Aze, T., Pearson, P. N., Dickson, A. J., Badger, M. P. S., Bown, P. R., Pancost, R. D., et al. (2014).
682 Extreme warming of tropical waters during the Paleocene-Eocene thermal maximum. *Geology*, 42,
683 739–742. <http://dx.doi.org/10.1130/G35637.1>
684
- 685 Azéma, J., Glaçon, G., & Tournon, J. (1981). Nouvelles données sur le Paléocène à Foraminifères
686 planctoniques de la bordure pacifique du Costa Rica. *Compte rendu sommaire des séances de la Société*
687 *géologique de France*, 3, 85–88.
688
- 689 Babila, T. L., Penman, D. E., Hönisch, B., Kelly, D. C., Bralower, T. J., Rosenthal, Y., & Zachos, J. C.
690 (2018). Capturing the global signature of surface ocean acidification during the Palaeocene-Eocene
691 Thermal Maximum. *Philosophical Transactions of the Royal Society A: Mathematical, Physical &*
692 *Engineering Sciences*, 376, 2017072. <https://doi.org/10.1098/rsta.2017.0072>
693
- 694 Bandini, A. N., Flores, K., Baumgartner, P. O., Jackett, S.-J., & Denyer, P. (2008). Late cretaceous and
695 Paleogene Radiolaria from the Nicoya Peninsula, Costa Rica: a tectonostratigraphic application.
696 *Stratigraphy*, 5, 3–21.
697
- 698 Baumgartner, P. O., Flores, K., Bandini, A. N., Girault, F., & Cruz, D. (2008). Upper Triassic to
699 Cretaceous radiolaria from Nicaragua and northern Costa Rica—The Mesquito composite oceanic
700 terrane. *Ofioliti*, 33, 1–19. <https://doi.org/10.4454/ofioliti.v33i1.356>
701
- 702 Baumgartner, P. O., Mora, C. R., Butterlin, J., Sigal, J., Glaçon, G., Azéma, J., & Bourgois, J. (1984).
703 Sedimentación y paleogeografía del Cretácico y Cenozoico del litoral pacífico de Costa Rica. *Revista*
704 *Geológica de América Central*, 1, 57–136. <https://doi.org/10.15517/rgac.v0i01.10469>
705
- 706 Baumgartner-Mora, C., & Baumgartner, P. O. (2016). Paleocene-earliest Eocene larger benthic
707 foraminifera and Ranikothalia-bearing carbonate paleo-environments of Costa Rica (South Central
708 America). *Micropaleontology*, 62, 453–508.
709

- 710 Baumgartner-Mora, C., Baumgartner, P. O., & Andjic, G. (2019). A new model: Punctuated Chlorozoan
711 Carbonates-biotic response to accretion tectonics and volcanism (Cretaceous-Cenozoic, Mid-America).
712 34th IAS Meeting of Sedimentology, Rome, Italy.
713
- 714 Berggren, W. A., Kent, D. V., Swisher, C. C., III, & Aubry, M.-P. (1995). A revised Cenozoic
715 geochronology and chronostratigraphy. In: Berggren, W.A., Kent, D.V., Aubry, M.-P., and Hardenbol,
716 J. Eds., *Geochronology, Time Scales and Global Stratigraphic Correlation. A Unified Temporal*
717 *Framework for a Historical Geology*, 129–212. Tulsa: *SEPM Special Publication*, 54.
718 <https://doi.org/10.2110/pec.95.04.0129>
719
- 720 Bishop, B. T., Beck, S. L., Zandt, G., Wagner, L., Long, M., Antonijevic, S. K., et al. (2017). Causes
721 and consequences of flat-slab subduction in southern Peru. *Geosphere*, 13(5), 1392–1407.
722 <https://doi.org/10.1130/GES01440.1>
723
- 724 Bornemann, A., Norris, R. D., Lyman, J. A., D’haenens, S., Groeneveld, J., Röhl, U., et al. (2014).
725 Persistent environmental change after the Paleocene–Eocene thermal maximum in the eastern North
726 Atlantic. *Earth and Planetary Science Letters*, 394, 70–81. <https://doi.org/10.1016/j.epsl.2014.03.017>
727
- 728 Bowring, J. F., McLean, N. M., & Bowring, S. A. (2012). Engineering cyber infrastructure for U-Pb
729 geochronology: Tripoli and U-Pb-Redux. *Geochemistry, Geophysics, Geosystems*, 12.
730 <https://doi.org/10.1029/2010GC003479>
731
- 732 Bralower, T. J., Kump, L. R., Self-Trail, J. M., Robinson, M. M., Lyons, S., Babila, T., et al. (2018).
733 Evidence for shelf acidification during the onset of the Paleocene-Eocene Thermal Maximum.
734 *Paleoceanography and Paleoclimatology*, 33, 1408–1426. <https://doi.org/10.1029/2018PA003382>
735
- 736 Buchs, D. M., Arculus, R. J., Baumgartner, P. O., Baumgartner-Mora, C., & Ulianov, A. (2010). Late
737 Cretaceous arc development on the SW margin of the Caribbean Plate: Insights from the Gofito, Costa
738 Rica, and Azuero, Panama, complexes. *Geochemistry, Geophysics, Geosystems*, 11, Q07S24,
739 <https://doi.org/10.1029/2009gc002901>
740
- 741 Calvo, C., & Bolz, A. (1991). La Formación Espíritu Santo (Costa Rica): sistema de plataforma
742 carbonatada autóctona del Paleoceno superior-Eoceno inferior. *Revista Geológica de América Central*,
743 13, 91–95. <https://doi.org/10.15517/rgac.v0i13.13079>
744
- 745 Carmichael, M. J., Lunt, D. J., Huber, M., Heinemann, M., Kiehl, J., LeGrande, A., et al. (2016). A
746 model–model and data–model comparison for the early Eocene hydrological cycle. *Climate of the Past*,
747 12(2), 455–481. <https://doi.org/10.5194/cp-12-455-2016>
748
- 749 Chesnel, V., López-Murillo, E., Löser, H., & Velázquez Heras, J.E. (2024). Puerto Nispero, a
750 Maastrichtian carbonate platform in Costa Rica. *Journal of South American Earth Sciences*, 141,
751 104953. <https://doi.org/10.1016/j.jsames.2024.104953>.
752
- 753 Clerc, C. (1998). Foraminifères planctoniques en sections de la couverture du terrain de Nicoya (Costa
754 Rica). Crétacé supérieur- Paléogène. Travail de diplôme, Université de Genève, 121 p.
755
- 756 Cloos, M. (1993). Lithospheric buoyancy and collisional orogenesis: Subduction of oceanic plateaus,
757 continental margins, island arcs, spreading ridges, and seamounts. *Geological Society of America*
758 *Bulletin*, 105, 715–737. [https://doi.org/10.1130/0016-7606\(1993\)105<0715:LBACOS>2.3.CO;2](https://doi.org/10.1130/0016-7606(1993)105<0715:LBACOS>2.3.CO;2)
759

- 760 Condon, D. J., Schoene, B., McLean, N. M., Bowring, S. A., & Parrish, R. (2015) Metrology and
761 traceability of U–Pb isotope dilution geochronology (EARTHTIME Tracer Calibration Part I).
762 *Geochimica et Cosmochimica Acta*, 164, 464–480. <https://doi.org/10.1016/j.gca.2015.05.026>
763
- 764 Colosimo, A. B., Bralower, T. J., & Zachos, J. C. (2006). Evidence for lysocline shoaling at the
765 Paleocene/Eocene Thermal Maximum on Shatsky Rise, northwest Pacific. In T.J. Bralower, I. Premoli
766 Silva, & M.J. Malone (Eds.), *Proceedings of the Ocean Drilling Program, Scientific Results*, 198:
767 College Station, TX (Ocean Drilling Program), 1–36. <https://doi.org/10.2973/odp.proc.sr.198.112.2006>
768
- 769 Corrigan, J., Mann, P., & Ingle, J. C. (1990). Forearc response to subduction of the Cocos Ridge,
770 Panama-Costa Rica. *Geological Society of America Bulletin*, 102, 628–652.
771 [https://doi.org/10.1130/0016-7606\(1990\)102<628:FRTSOT>2.3.CO;2](https://doi.org/10.1130/0016-7606(1990)102<628:FRTSOT>2.3.CO;2)
772
- 773 Dengo, G. (1962). *Estudio Geológico de la Región de Guanacaste*. Instituto Geografico Nacional, San
774 José, Costa Rica, 112 p.
775
- 776 Denizot, M. (1968). *Les Algues Floridées Encrustantes (à l'exclusion des Corallinacées)*. Laboratoire
777 de Cryptogamie, Musée National d'Histoire Naturelle de Paris, 310 p.
778
- 779 Denyer, P. (2019). *Perspectiva geológica del noroeste de Costa Rica: Historia, evolución y cartografía*.
780 San José, Costa Rica. Editorial Universidad de Costa Rica, 347 pages and 18 maps at 1:50,000 scale.
781
- 782 Denyer, P., & Alvarado, G. E. (2007). *Mapa Geológico de Costa Rica 1:400'000*. Librería Francesa
783 S.A.
784
- 785 Denyer, P., Aguilar, T., & Montero, W. (2014a) *Cartografía geológica de la Península de Nicoya, Costa*
786 *Rica: Estratigrafía y tectónica*: San José, Costa Rica, Editorial Universidad de Costa Rica, 207 p.
787
- 788 Denyer, P., Aguilar, T., & Montero, W. (2014b). *Cartografía geológica de la Península de Nicoya, Costa*
789 *Rica: Mapas geológicos*: San José, Costa Rica, Editorial Universidad de Costa Rica, scale 1:50,000, 21
790 sheets.
791
- 792 Dickens, G. R., Castillo, M. M., & Walker, J. C. G. (1997). A blast of gas in the latest Paleocene:
793 Simulating first-order effects of massive dissociation of oceanic methane hydrate. *Geology*, 25(3), 259–
794 262. [https://doi.org/10.1130/0091-7613\(1997\)025<259:ABOGIT>2.3.CO;2](https://doi.org/10.1130/0091-7613(1997)025<259:ABOGIT>2.3.CO;2)
795
- 796 Di Marco, G., Baumgartner, P. O., & Chanell, J. E. T. (1995). Late Cretaceous-Early Tertiary
797 paleomagnetic data and a revised tectonostratigraphic subdivision of Costa Rica and western Panama.
798 In P. Mann (Ed.) *Geologic and tectonic development of the Caribbean Plate Boundary in Southern*
799 *Central America. Geological Society of America Special Papers*, 295, 1–27.
800 <https://doi.org/10.1130/SPE295-p1>
801
- 802 Dorobek, S.L. (2008). Carbonate-platform facies in volcanic-arc settings: characteristics and controls
803 on deposition and stratigraphic development. In: A. E. Draut, P. D. Clift, & D. W. Scholl (Eds.)
804 *Formation and applications of the sedimentary record in Arc Collision Zones. Geological Society of*
805 *America Special Papers*, 463, 55–90. [https://doi.org/10.1130/2008.2436\(04\)](https://doi.org/10.1130/2008.2436(04))
806
- 807 Egger, H., Heilmann-Clausen, C., & Schmitz, B. (2000). The Paleocene/Eocene-boundary interval of a
808 Tethyan deep-sea section (Austria) and its correlation with the North Sea basin. *Bulletin de la Société*
809 *Géologique de France*, 171(2), 207–216. <https://doi.org/10.2113/171.2.207>
810

- 811 Escalante, G. (1991). The geology of southern Central America and western Colombia. In G. Dengo &
812 J. E. Case (Eds.), *The geology of North America: The Caribbean region, The Decade of North American*
813 *Geology. Geological Society of America, H*, 201–230. <https://doi.org/10.1130/DNAG-GNA-H.201>
814
- 815 Escalona, A., Norton, I. O., Lawver, L. A., & Gahagan, L. (2021). Quantitative Plate Tectonic
816 Reconstructions of the Caribbean Region from Jurassic to Present. In C. Bartolini (Ed.) *South America-*
817 *Caribbean-Central Atlantic Plate Boundary. American Association of Petroleum Geologists Memoir,*
818 *123*, 239–263. <https://doi.org/10.1306/13692247M1233849>
819
- 820 Escuder-Viruete, J., Baumgartner, P. O., & Castillo-Carrión, M. (2015). Compositional diversity in
821 ophiolitic peridotites as result of a multi-process history: The Santa Elena ophiolite, northwest Costa
822 Rica. *Lithos*, *231*, 16–34. <https://doi.org/10.1016/j.lithos.2015.05.019>
823
- 824 Flores, K. (2006). Jurassic–Late Cretaceous oceanic crustal terranes and arc-derived sediments south
825 Chortis Block (NE Nicaragua to NW Costa Rica). Preliminary results of two key areas: Nicoya
826 Peninsula and Siuna District. D.E.A. thesis, Lausanne, Switzerland, University of Lausanne, 107 p.
827
- 828 Flores, K. (2009). Mesozoic Oceanic Terranes of Southern Central America: Geology, Geochemistry
829 and Geodynamics Ph.D. thesis Lausanne, Switzerland, University of Lausanne, 290 p.
830
- 831 Flores, K., Denyer, P., & Aguilar, T. (2003a). Nueva propuesta estratigráfica: Geología de las hojas
832 Matambú y Talolinga, Guanacaste, Costa Rica. *Revista Geológica de América Central*, *28*, 131–138.
833 <https://doi.org/10.15517/rgac.v0i28.7793>
834
- 835 Flores, K., Denyer, P., & Aguilar, T. (2003b). Nueva propuesta estratigráfica: Geología de la hoja
836 Abangares, Guanacaste, Costa Rica. *Revista Geológica de América Central*, *29*, 127–136.
837 <https://doi.org/10.15517/rgac.v0i29.7780>
838
- 839 Frisch, W., Meschede, M., & Blakey, R. (2011). Subduction zones, island arcs and active continental
840 margins. In W. Frisch, M. Meschede, & R. Blakey (Eds.), *Plate Tectonics*. Springer, Berlin, Heidelberg,
841 91–122. https://doi.org/10.1007/978-3-540-76504-2_7
842
- 843 Gardner, T. W., Fisher, D. M., Morell, K. D., & Cupper, M. L. (2013). Upper-plate deformation in
844 response to flat slab subduction inboard of the aseismic Cocos Ridge, Osa Peninsula, Costa Rica.
845 *Lithosphere*, *5*, 247–264. <https://doi.org/10.1130/L251.1>
846
- 847 Gerstenberger, H., & Haase, G. (1997). A highly effective emitter substance for mass spectrometric Pb
848 isotope ratio determinations. *Chemical Geology*, *136*, 309–312. [https://doi.org/10.1016/S0009-](https://doi.org/10.1016/S0009-2541(96)00033-2)
849 [2541\(96\)00033-2](https://doi.org/10.1016/S0009-2541(96)00033-2)
850
- 851 Gibbs, S. J., Stoll, H. M., Bown, P. R., & Bralower, T. J. (2010). Ocean acidification and surface water
852 carbonate production across the Paleocene-Eocene Thermal Maximum. *Earth Planet. Sci. Lett.*, *295*(3–
853 *4)*, 583–592. <https://doi.org/10.1016/j.epsl.2010.04.044>
854
- 855 Giusberti, L., Rio, D., Agnini, C., Backman, J., Fornaciari, E., Tateo, F., & Oddone, M. (2007). Mode
856 and tempo of the Paleocene-Eocene thermal maximum in an expanded section from the Venetian pre-
857 Alps. *Geological Society of America Bulletin*, *119*, 391–412. <https://doi.org/10.1130/B25994.1>
858
- 859 Handley, L., O'Halloran, A., Pearson, P. N., Hawkins, E., Nicholas, C. J., Schouten, S., et al. (2012).
860 Changes in the hydrological cycle in tropical East Africa during the Paleocene Eocene Thermal

- 861 Maximum. *Palaeogeography, Palaeoclimatology, Palaeoecology*, 329, 10–21.
862 <http://dx.doi.org/10.1016/j.palaeo.2012.02.002>
863
- 864 Hiess, J., Condon, D. J., McLean, N. & Noble, S. R. (2012). 238U/235U systematics in terrestrial
865 uranium-bearing minerals. *Science*, 335, 1610–1614. <https://doi.org/10.1126/science.1215507>
866
- 867 Huber B.T., Petrizzo M.R., Young J.R., Falzoni F., Gilardoni S.E, Bown P.R., & Wade B.S. (2016).
868 Pforams@mikrotax: A new online taxonomic database for planktonic foraminifera. *Micropaleontology*,
869 62(6), 429–438. <https://doi.org/10.47894/mpal.62.6.02>
870
- 871 Immenhauser, A. (2022). On the delimitation of the carbonate burial realm. *The Depositional Record*,
872 8, 524–574. <https://doi.org/10.1002/dep2.173>
873
- 874 Jaccard, S., & Münster, M. (2001). Etude géologique multidisciplinaire de la plateforme de Barra Honda
875 (Guanacaste, Costa Rica): Sédimentologie, isotopes stables du strontium, du carbone, de l'Oxygène et
876 contexte géodynamique. D.E.A. thesis, Université de Lausanne, Lausanne, Switzerland, 98 p.
877
- 878 Jaccard, S., Münster, M., Baumgartner, P. O., Baumgartner-Mora, C., & Denyer, P. (2001). Barra
879 Honda (Upper Paleocene-Lower Eocene) and El Viejo (Campanian-Maastrichtian) carbonate platforms
880 in the Tempisque area (Guanacaste, Costa Rica). *Revista Geológica de América Central*, 24, 9–28.
881 <https://doi.org/10.15517/rgac.v0i24.8550>
882
- 883 Jackett, S.-J., Baumgartner, P. O., & Bandini, A. N. (2008). A new low-latitude Late Paleocene-Early
884 Eocene radiolarian biozonation based on unitary associations: applications for accreted terranes.
885 *Stratigraphy*, 5(1), 39–62.
886
- 887 Jiang, M.-J., & Robinson, E. (1987). Calcareous nannofossils and larger Foraminifera in Jamaican rocks
888 of Cretaceous to early Eocene age. In: Ahmad R. (Ed.), Proceedings of a workshop on the status of
889 Jamaican geology. Geological Society of Jamaica, Signart Printing House, Kingston, Jamaica, 24–51.
890
- 891 Kelly, D. C., Bralower, T. J., Zachos, J. C., Premoli Silva, I., & Thomas, E. (1996). Rapid
892 diversification of planktonic foraminifera in the tropical Pacific (ODP Site 865) during the late
893 Paleocene thermal maximum. *Geology*, 24, 423–426. [https://doi.org/10.1130/0091-7613\(1996\)024<0423:RDOPFI>2.3.CO;2](https://doi.org/10.1130/0091-7613(1996)024<0423:RDOPFI>2.3.CO;2)
894
895
- 896 Kemp, D. B., & Sadler, P. M. (2014). Climatic and eustatic signals in a global compilation of shallow
897 marine carbonate accumulation rates. *Sedimentology*, 61, 1286–1297.
898 <https://doi.org/10.1111/sed.12112>
899
- 900 Klug, H. P., & Alexander, L. E. (1974). X-Ray Diffraction Procedures: For Polycrystalline and
901 Amorphous Materials. John Wiley and Sons, New-York, 992 p.
902
- 903 Kopp, R. E., Schumann, D., Raub, T. D., Powars, D. S., Godfrey, L. V., Swanson-Hysell, N. L., et al.
904 (2009). An Appalachian Amazon? Magnetofossil evidence for the development of a tropical river-like
905 system in the mid- Atlantic United States during the Paleocene-Eocene thermal maximum.
906 *Paleoceanography*, 24, 1–17. <http://dx.doi.org/10.1029/2009PA001783>
907
- 908 Kübler, B. (1983). Dosage quantitatif des minéraux majeurs des roches sédimentaires par diffraction X.
909 Cahier de l'institut de Géologie de Neuchâtel, Série AX (1.1-1.2), 1–13.
910

- 911 Ludwig, K.R. (1991). ISOPLOT for MS-DOS, a plotting and regression program for radiogenic isotope
912 data, for IBM-PC compatible computers, version 2.75. *U.S. Geological Survey, Open-File Report 91-*
913 *445*, 45 p. <https://doi.org/10.3133/ofr91445>
914
- 915 Lundberg, N. (1982). Evolution of the slope landward of the Middle America Trench, Nicoya Peninsula,
916 Costa Rica. In J. K. Leggett (Ed.) *Trench-forearc geology. Geological Society, London, Special*
917 *Publications, 10*, 131–147. <https://doi.org/10.1144/GSL.SP.1982.010.01.9>
918
- 919 Lyle, M., Wilson, P. A. & Janecek, T. R. (2002). Leg 199 summary. *Proceedings of the Ocean Drilling*
920 *Program, Initial Reports, 199*, 1–87. <https://doi.org/10.2973/odp.proc.ir.199.101.2002>
921
- 922 Mann, P. (2007). Overview of the tectonic history of northern Central America. In P. Mann (Ed.),
923 *Geologic and tectonic development of the Caribbean plate boundary in northern Central America.*
924 *Geological Society of America Special Papers, 428*, 1–19. [https://doi.org/10.1130/2007.2428\(01\)](https://doi.org/10.1130/2007.2428(01))
925
- 926 Massieux, M., & Denizot, M. (1964). Rapprochement du genre *Pseudolithothamnium* Pfender avec le
927 genre actuel *Ethelia* Weber Van Bosse (Algues Florideae, Squamariaceae). *Revue de*
928 *Micropaléontologie, 7*, 31–42.
929
- 930 McGeary, S., Nur, A., & Benavraham, Z. (1985). Spatial Gaps in Arc Volcanism: The Effect of
931 Collision or Subduction of Oceanic Plateaus. *Tectonophysics, 119*, 195–221.
932 [https://doi.org/10.1016/0040-1951\(85\)90039-3](https://doi.org/10.1016/0040-1951(85)90039-3)
933
- 934 McInerney, F. A., & Wing, S. L. (2011). The Paleocene-Eocene Thermal Maximum: A perturbation of
935 carbon cycle, climate, and biosphere with implications for the future. *Annual Review of Earth and*
936 *Planetary Sciences, 39*, 489–516. <https://doi.org/10.1146/annurev-earth-040610-133431>
937
- 938 McLean, N. M., Bowring, J. F., & Bowring, S. A. (2011). An algorithm for U-Pb isotope dilution data
939 reduction and uncertainty propagation. *Geochemistry, Geophysics, Geosystems, 12*, Q0AA18.
940 <https://doi.org/10.1029/2010GC003478>
941
- 942 McLean, N. M., Condon, D. J., Schoene, B., & Bowring, S. A. (2015). Evaluating uncertainties in the
943 calibration of isotopic reference materials and multi-element isotopic tracers (EARTHTIME Tracer
944 Calibration Part II). *Geochimica et Cosmochimica Acta, 164*, 481–501.
945 <https://doi.org/10.1016/j.gca.2015.02.040>
946
- 947 Meffre, S., & Crawford, A. J. (2001). Collision tectonics in the New Hebrides arc (Vanuatu). *Island*
948 *Arc, 10*, 33–50. <https://doi.org/10.1046/j.1440-1738.2001.00292.x>
949
- 950 Miller, K. G., Browning, J. V., Schmelz, W. J., Kopp, R. E., Mountain, G. S., & Wright, J. D. (2020).
951 Cenozoic sea-level and cryospheric evolution from deep-sea geochemical and continental margin
952 records. *Science Advances, 6*(20), eaaz1346. <https://doi.org/10.1126/sciadv.aaz1346>
953
- 954 Miller, K. G., Kominz, M. A., Browning, J. V., Wright, J. D., Mountain, G. S., Katz, M. E., et al. (2005).
955 The Phanerozoic record of global sealevel change. *Science, 310*, 1293–1298. <https://doi.org/10.1126/science.1116412>
956
957
- 958 Molina, E., Arenillas, I., & Pardo, A. (1999). High resolution planktic foraminiferal biostratigraphy and
959 correlation across the Paleocene/Eocene boundary in the Tethys. *Bulletin de la Société Géologique de*
960 *France, 170*, 521–530.
961

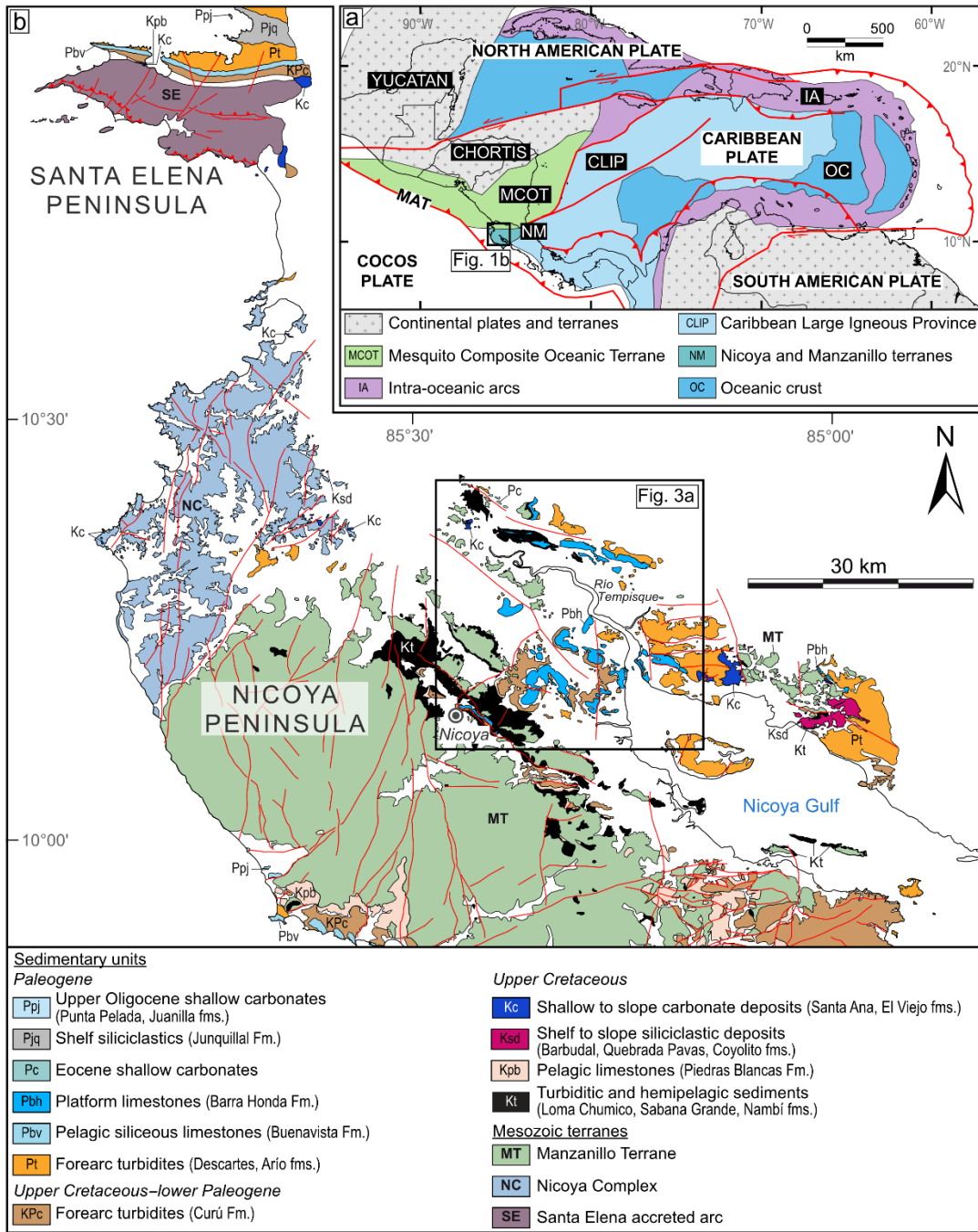
- 962 Mora, S. (1981). Barra Honda. Editorial Universidad Estatal a Distancia, Serie Educación Ambiental,
963 5, San José, 115 p.
964
- 965 Mora, C., & Baumgartner, P. O. (1985). Mapa geológico del sur de la península de Nicoya. Escala 1:50
966 000. Instituto Geografico Nacional Rica, San José, Costa Rica.
967
- 968 Murphy, B. H., Farley, K. A., & Zachos, J. C. (2010). An extraterrestrial He-3-based timescale for the
969 Paleocene-Eocene Thermal Maximum (PETM) from Walvis Ridge, IODP Site 1266. *Geochimica et*
970 *Cosmochimica Acta*, 74(17), 5098–5108. <https://doi.org/10.1016/j.gca.2010.03.039>
971
- 972 Murphy, M.A., & Salvador A. (1999). International stratigraphic guide—an abridged edition. *Episodes*,
973 22, 255–271. <https://doi.org/10.18814/epiiugs/1999/v22i4/002>
974
- 975 Muttoni, G., & Kent, D.V. (2007). Widespread formation of cherts during the early Eocene climate
976 optimum. *Palaeogeography, Palaeoclimatology, Palaeoecology*, 253, 348–362.
977 <https://doi.org/10.1016/j.palaeo.2007.06.008>
978
- 979 Olsson, R. K., Hemleben, C., Berggren, W. A., & Huber, B. T. (1999). Atlas of Paleocene Planktonic
980 Foraminifera. *Smithsonian Contributions to Paleobiology*, 85, 252 p.
981 <https://doi.org/10.5479/si.00810266.85.1>
982
- 983 Pak, D. K., & Miller, K. G. (1992). Paleocene to Eocene benthic foraminiferal isotopes and
984 assemblages: Implications for deepwater circulation. *Paleoceanography*, 7(4), 405–422.
985 <https://doi.org/10.1029/92PA01234>
986
- 987 Patino, L. C., Alvarado-Induni, G. E., & Vogel, T. A. (2004). Early arc magmatism: Geochemical
988 characteristics of volcanic clasts from Punta Sámará, Costa Rica. *Revista Geológica de América*
989 *Central*, 30, 117–125. <https://doi.org/10.15517/rgac.v0i30.7279>
990
- 991 Pearson, P. N., Olsson, R. K., Huber, B. T., Hemleben, C., & Berggren, W.A. (2006). Atlas of Eocene
992 Planktonic foraminifera. *Cushman Foundation Special Publication*, 41, 514 p.
993
- 994 Penman, D. E. (2016). Silicate weathering and North Atlantic silica burial during the Paleocene-Eocene
995 Thermal Maximum. *Geology*, 44(9), 731–734. <https://doi.org/10.1130/G37704.1>
996
- 997 Penman, D. E., Honisch, B., Zeebe, R. E., Thomas, E., & Zachos, J. C. (2014). Rapid and sustained
998 surface ocean acidification during the Paleocene-Eocene Thermal Maximum. *Paleoceanography*, 29,
999 357–369. <https://doi.org/10.1002/2014PA002621>
1000
- 1001 Penman, D. E., Keller, A., D'haenens, S., Kirtland Turner, S., & Hull, P. M. (2019). Atlantic deep-sea
1002 cherts associated with Eocene hyperthermal events. *Paleoceanography and Paleoclimatology*, 34, 287–
1003 299. <https://doi.org/10.1029/2018PA003503>
1004
- 1005 Petrizzo M.R., Wade B.S., & Gradstein F.M. (2020). Planktonic foraminifera. In *Geologic Time Scale*
1006 *2020*, Eds. F.M. Gradstein, J.G. Ogg, M.D. Schmitz, G.M. Ogg, 2 volume set, ISBN: 978-0-12-824360-
1007 2, 1390 pp., doi.org/10.1016/C2020-1-02369-3. Vol. 1, chapter 3 Evolution and biostratigraphy,
1008 subchapter 3G, 74-87. Elsevier B.V. <https://doi.org/10.1016/B978-0-12-824360-2.00003-6>
1009
- 1010 Pindell, J. L., & Kennan, L. (2009). Tectonic evolution of the Gulf of Mexico, Caribbean and northern
1011 South America in the mantle reference frame: an update. In K. H. James, M. A. Lorente & J. L. Pindell

- 1012 (Eds.), The origin and evolution of the Caribbean Plate. *Geological Society, London, Special*
1013 *Publications*, 328, 1–55. <https://doi.org/10.1144/SP328>
- 1014
- 1015 Pfender, J. (1936). Sur un organisme constructeur des calcaires créacés et nummulitiques,
1016 Pseudolithothamnium album, n. g. nov. sp. *Bulletin de la Société Géologique de France*, 6, 303–308.
- 1017
- 1018 Praturlon, A. (1966). Algal assemblages from Lias to Paleocene in Southern Latium-Abruzzi: a review.
1019 *Bollettino della Società Geologica Italiana*, 85, 167–194.
- 1020
- 1021 Ranero, C. R., Villasenor, A., Phipps Morgan, J., & Weinrebe, W. (2005). Relationship between bend-
1022 faulting at trenches and intermediate-depth seismicity. *Geochemistry, Geophysics, Geosystems*, 6,
1023 Q12002. <https://doi.org/10.1029/2005GC000997>
- 1024
- 1025 Rivier, F. (1983). Síntesis geológica y mapa geológico del area del Bajo Tempisque Guanacaste, Costa
1026 Rica. Instituto Geografico Nacional, Informe semestral, Costa Rica, 7–30.
- 1027
- 1028 Robinson, E., & Wright, R. M. (1993). Jamaican Paleogene larger foraminifera. In R. M. Wright & E.
1029 Robinson, E. (Eds.), Biostratigraphy of Jamaica. *Geological Society of America Memoir*, 182, 283–345.
1030 <https://doi.org/10.1130/MEM182-p283>
- 1031
- 1032 Romito, S., & Mann, P. (2020). Tectonic terranes underlying the present-day Caribbean plate: Their
1033 tectonic origin, sedimentary thickness, subsidence histories, and regional controls on hydrocarbon
1034 resources. *Geological Society, London, Special Publications*, 504, 343–377.
1035 <https://doi.org/10.1144/SP504-2019-221>
- 1036
- 1037 Rogers, R. D., Mann, P., & Emmet, P. A. (2007). Tectonic terranes of the Chortis block based on
1038 integration of regional aeromagnetic and geologic data. In P. Mann (Ed.), Geologic and tectonic
1039 development of the Caribbean plate in northern Central America. *Geological Society of America Special*
1040 *Papers*, 428, 65–88. [https://doi.org/10.1130/2007.2428\(04\)](https://doi.org/10.1130/2007.2428(04))
- 1041
- 1042 Rosenbaum, G., & Mo, W. (2011). Tectonic responses to the subduction of high bathymetric relief.
1043 *Gondwana Research*, 19, 571–582. <https://doi.org/10.1016/j.gr.2010.10.007>
- 1044
- 1045 Sanchez, J., Mann, P., Carvajal-Arenas, L. C., & Bernal-Olaya, R. (2019). Regional transect across the
1046 western Caribbean Sea based on integration of geologic, seismic reflection, gravity, and magnetic data:
1047 *Bulletin of the American Association of Petroleum Geologists*, 103(2), 303–343.
1048 <https://doi.org/10.1306/05111816516>
- 1049
- 1050 Schaltegger, U., Ovtcharova, M., Gaynor, S. P., Schoene, B., Wotzlaw, J.-F., Davies, J. F., et al. (2021).
1051 Long-term repeatability and interlaboratory reproducibility of high-precision ID-TIMS U–Pb
1052 geochronology. *Journal of Analytical Atomic Spectrometry*, 36(7), 1466–1477.
1053 <https://doi.org/10.1039/D1JA00116G>
- 1054
- 1055 Scheibner, C., & Speijer, R. P. (2008). Late Paleocene–early Eocene Tethyan carbonate platform
1056 evolution—A response to long- and short-term paleoclimatic change. *Earth-Science Reviews*, 90, 71–
1057 102. <https://doi.org/10.1016/j.earscirev.2008.07.002>
- 1058
- 1059 Schmitz, B., Pujalte, V., & Nunez-Betelu, K. (2001). Climate and sea-level perturbations during the
1060 initial Eocene thermal maximum: evidence from siliciclastic units in the Basque Basin (Ermua, Zumaia
1061 and Trabakua Pass), northern Spain. *Palaeogeography, Palaeoclimatology, Palaeoecology*, 165, 299–
1062 320. [https://doi.org/10.1016/S0031-0182\(00\)00167-X](https://doi.org/10.1016/S0031-0182(00)00167-X)

1063
1064
1065
1066
1067
1068
1069
1070
1071
1072
1073
1074
1075
1076
1077
1078
1079
1080
1081
1082
1083
1084
1085
1086
1087
1088
1089
1090
1091
1092
1093
1094
1095
1096
1097
1098
1099
1100
1101
1102
1103
1104
1105
1106
1107
1108
1109
1110
1111

- Schmitz, M. D., & Schoene, B. (2007). Derivation of isotope ratios, errors, and error correlations for U-Pb geochronology using ^{205}Pb - ^{235}U -(^{233}U)-spiked isotope dilution thermal ionization mass spectrometric data. *Geochemistry, Geophysics, Geosystems*, 8. <https://doi.org/10.1029/2006GC001492>
- Schoene, B., Crowley, J. L., Condon, D. J., Schmitz, M. D., & Bowring, S. A. (2006). Reassessing the uranium decay constants for geochronology using ID-TIMS U-Pb data. *Geochimica et Cosmochimica Acta*, 70, 426–445. <https://doi.org/10.1016/j.gca.2005.09.007>
- Sluijs, A., Brinkhuis, H., Crouch, E. M., John, C. M., Handley, L., Munsterman, D., et al., (2008). Eustatic variations during the Paleocene-Eocene greenhouse world. *Paleoceanography*, 23, PA4216, <https://doi.org/10.1029/2008PA001615>
- Sluijs, A., Schouten, S., Pagani, M., Woltering, M., Brinkhuis, H., Damsté, J. S. P., et al. (2006). Subtropical Arctic Ocean temperatures during the Palaeocene/Eocene Thermal Maximum. *Nature*, 441, 610–613. <https://doi.org/10.1038/nature04668>
- Speijer, R. P., Pälike, H., Hollis, C. J., Hooker, J. J., & Ogg, J. G. (2020). The Paleogene Period. In F. M. Gradstein, J. G. Ogg, M. D. Schmitz, & G. M. Ogg (Eds.), *Geologic Time Scale 2020*. Elsevier 1087–1140. <https://doi.org/10.1016/B978-0-12-824360-2.00028-0>
- Spikings, R., & Simpson, G. (2014). Rock uplift and exhumation of continental margins by the collision, accretion, and subduction of buoyant and topographically prominent oceanic crust. *Tectonics*, 33, 635–655. <https://doi.org/10.1002/2013TC003425>
- Spötl, C., & Vennemann, T. W. (2003). Continuous-flow IRMS analysis of carbonate minerals. *Rapid Communications in Mass Spectrometry*, 17, 1004–1006. <https://doi.org/10.1002/rcm.1010>
- Sprechmann, P. (1982). Estratigrafía de Costa Rica I: Unidades estratigráficas sedimentarias. 5th Latinamerican Geological Congress, Argentina.
- Sprechmann, P. (1984). Manual de geología de Costa Rica: estratigrafía. 320 p. Editorial Universidad de Costa Rica.
- Struss, I., Artiles, V., Cramer, B., & Winsemann, J. (2008). The petroleum system in the Sandino Forearc Basin, offshore western Nicaragua. *Journal of Petroleum Geology*, 31, 221–244. <https://doi.org/10.1111/j.1747-5457.2008.00418.x>
- Tetreault, J. L., & Buitter, S. (2012). Geodynamic models of terrane accretion: testing the fate of island arcs, oceanic plateaus, and continental fragments in subduction zones. *Journal of Geophysical Research*, 117, B08403. <https://doi.org/10.1029/2012JB009316>
- Vogt, K., & Gerya, T. V. (2014). From oceanic plateaus to allochthonous terranes: Numerical modelling. *Gondwana Research*, 25, 494–508. <https://doi.org/10.1016/j.gr.2012.11.002>
- von Huene, R., & Suess, E. (1988). Ocean Drilling Program Leg 112, Peru continental margin: Part 1, Tectonic history. *Geology*, 16 (10): 934–938. [https://doi.org/10.1130/0091-7613\(1988\)016<0934:ODPLPC>2.3.CO;2](https://doi.org/10.1130/0091-7613(1988)016<0934:ODPLPC>2.3.CO;2)

- 1112 Wade, B. S., O'Neill, J. F., Phujareanchaiwon, C., Ali, I., Lyle, M., & Witkowski, J. (2020). Evolution
1113 of deep-sea sediments across the Paleocene-Eocene and Eocene-Oligocene boundaries. *Earth-Science*
1114 *Reviews*, 211, 103403. <https://doi.org/10.1016/j.earscirev.2020.103403>
1115
- 1116 Wade, B. S., Pearson, P. N., Berggren, W. A., & Pälike, H. (2011). Review and revision of Cenozoic
1117 tropical planktonic foraminiferal biostratigraphy and calibration to the geomagnetic polarity and
1118 astronomical time scale. *Earth-Science Reviews*, 104(1–3), 111–142.
1119 <https://doi.org/10.1016/j.earscirev.2010.09.003>
1120
- 1121 Watanabe, T. K., Watanabe, T., Yamazaki, A., Pfeiffer, M., Garbe-Schönberg, D., & Claereboudt, M.
1122 R. (2017). Past summer upwelling events in the Gulf of Oman derived from a coral geochemical record.
1123 *Scientific Reports*, 7(1), 4568. <https://doi.org/10.1038/s41598-017-04865-5>
1124
- 1125 Weber, P. (2013). Assessing sedimentary evolution by means of Sr-isotope ratios: 3 case studies on the
1126 Caribbean Plate (Cretaceous: Nicoya Peninsula, Costa Rica, Tertiary: Hess Rise, and La Désirade,
1127 Guadeloupe, France). Ph.D. thesis, University of Lausanne, Lausanne, Switzerland, 176 p.
1128
- 1129 Weyl, R. (1980). *Geology of Central America*. Berlin, Gebrüder Borntraeger, 371 p.
1130
- 1131 Winguth, A. M., Thomas, E., & Winguth, C. (2012). Global decline in ocean ventilation, oxygenation,
1132 and productivity during the Paleocene-Eocene thermal maximum: implications for the benthic
1133 extinction. *Geology*, 40(3), 263–266. <https://doi.org/10.1130/G32529.1>
1134
- 1135 Young, A., Flament, N., Maloney, K., Williams, S., Matthews, K., Zahirovic, S., & Müller, R. D.
1136 (2019). Global kinematics of tectonic plates and subduction zones since the late Paleozoic Era.
1137 *Geoscience Frontiers*, 10, 989–1013. <https://doi.org/10.1016/j.gsf.2018.05.011>
1138
- 1139 Zachos, J. C., Kroon, D., Blum, P., et al. (2004). Proceedings of the Ocean Drilling Program, Scientific
1140 Results, Initial Reports, 208: College Station, TX (Ocean Drilling Program).
1141 <https://doi.org/10.2973/odp.proc.ir.208.2004>
1142
- 1143 Zachos, J. C., Rohl, U., Schellenberg, S. A., Sluijs, A., Hodell, D. A., Kelly, D. C., et al. (2005). Rapid
1144 acidification of the ocean during the Paleocene-Eocene Thermal Maximum. *Science*, 308(5728), 1611–
1145 1615. <https://doi.org/10.1126/science.1109004>
1146
- 1147 Zeebe, R. E., & Lourens, L. J. (2019). Solar System chaos and the Paleocene–Eocene boundary age
1148 constrained by geology and astronomy. *Science*, 365(6456), 926–929.
1149 <https://doi.org/10.1126/science.aax0612>
1150
- 1151 Zeebe, R. E., & Zachos, J. C. (2007). Reversed deep-sea carbonate ion basin gradient during Paleocene-
1152 Eocene Thermal Maximum. *Paleoceanography*, 22, PA3201. <https://doi.org/10.1029/2006PA001395>
1153
- 1154 Zoppis Bracci, L., & Del Giudice, D. (1958). Geología de la costa del Pacifico de Nicaragua. *Boletín*
1155 *del Servicio Geológico Nacional de Nicaragua*, 2, 19–68.
1156
1157
1158
1159
1160
1161
1162



1164

1165 **Figure 1.** (a) Plate tectonic map illustrating the main units of the Caribbean Plate (modified after
 1166 Baumgartner et al., 2008; Andjić et al., 2019b; Sanchez et al., 2019; Escalona et al., 2021; Romito &
 1167 Mann, 2021). MAT = Middle America Trench. (b) Geological map of northwestern Costa Rica,
 1168 centered on the Nicoya Peninsula (modified after Baumgartner et al., 1984; Mora & Baumgartner, 1985;
 1169 Flores et al., 2003a, 2003b; Flores, 2006; Denyer & Alvarado, 2007; Bandini et al., 2008; Flores, 2009;
 1170 Weber, 2013; Denyer et al., 2014b; Escuder-Viruet et al., 2015; Andjić et al., 2016, 2018a, 2019a).

1171

1172

1173

1174

1175

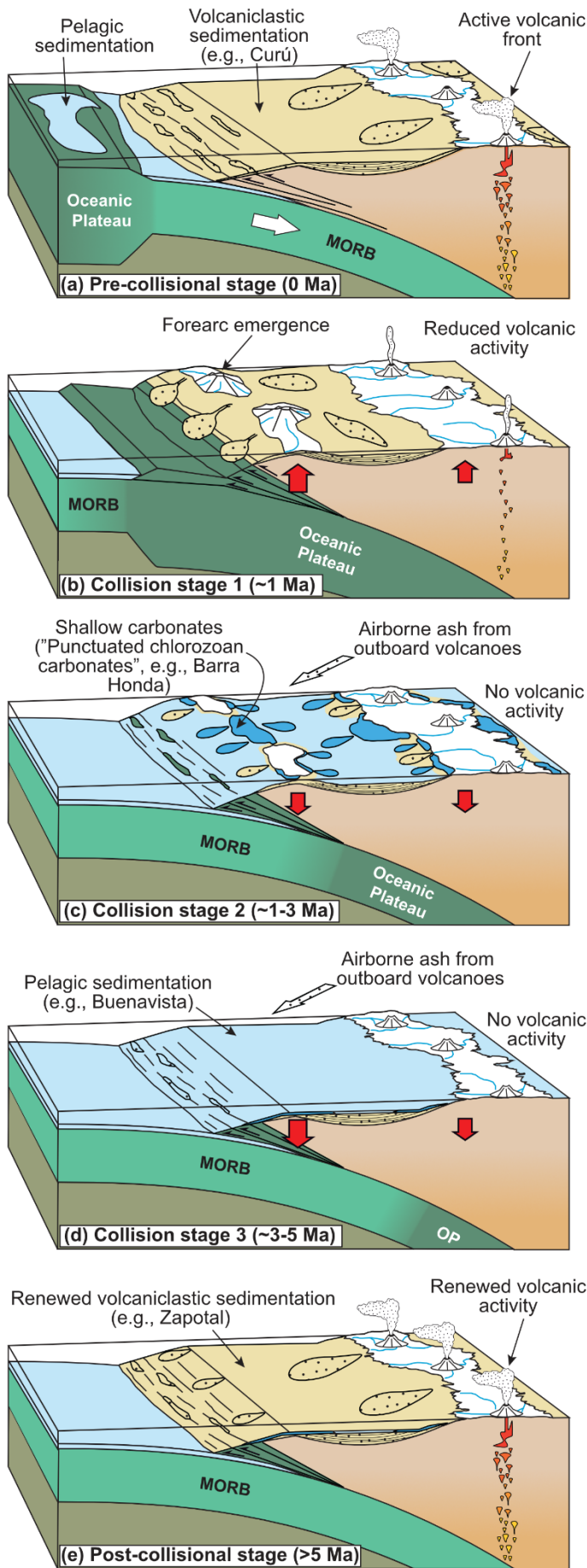
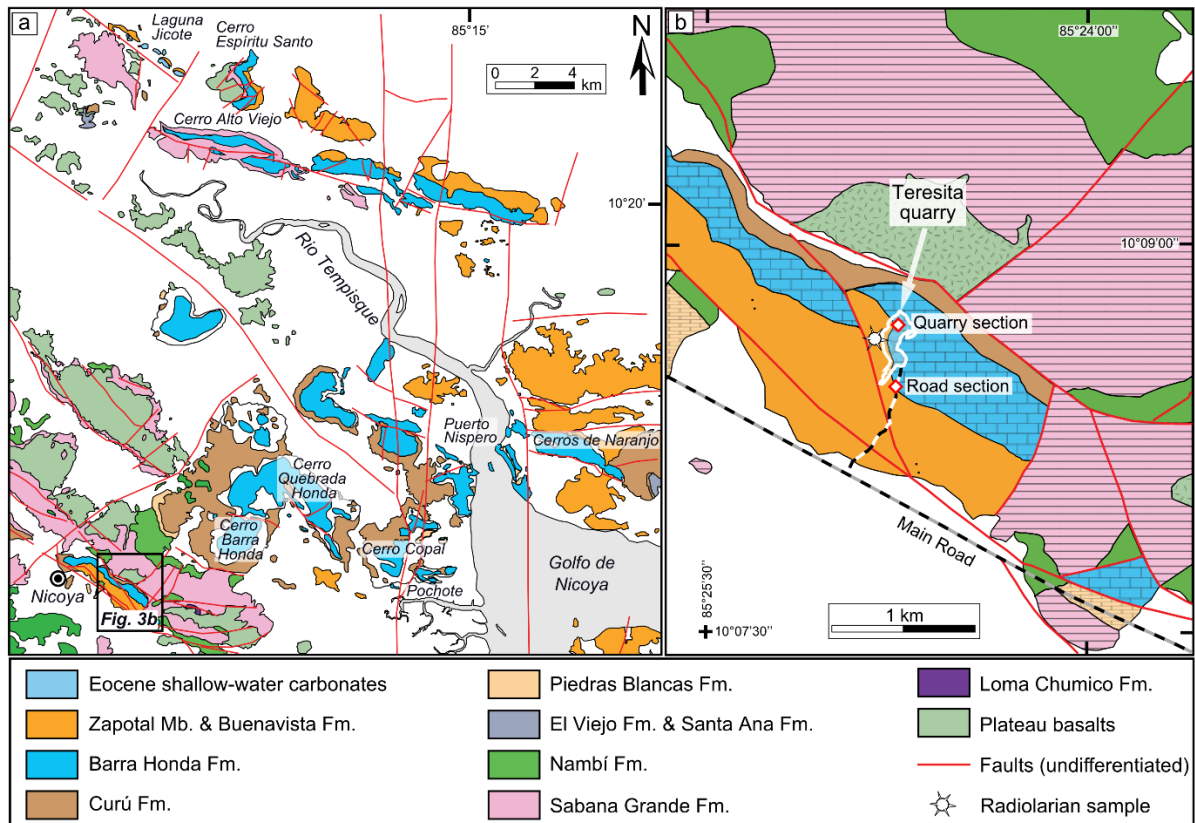


Figure 2. Formation and demise of carbonate shoals in response to rough crust subduction and arc extinction. The model is based on plateau collision events discussed in Baumgartner-Mora and Baumgartner (2016) and Andjić et al. (2016, 2018a, 2018b, 2019a). The drawing style is after Frisch et al. (2011). (a) Subduction of normal oceanic crust (labelled as MORB—Mid-oceanic ridge basalt) leads to arc volcanic activity. (b) Subduction of the bathymetric feature causes surface uplift in the forearc and progressive cessation of volcanic activity as the leading edge of the bathymetric feature reaches the window of major slab dehydration. Input of eroded detrital material and ongoing surface uplift hamper the formation and preservation of shallow-water carbonates. (c) Low forearc subsidence due to renewed subduction of normal oceanic crust at shallow depth. Ongoing subduction of the trailing edge of the bathymetric feature in the window of major slab dehydration sustains volcanic quiescence. The subsidence of the forearc and the reduced volcaniclastic input allow the short-lived development of shallow-water carbonate shoals (e.g., Barra Honda). (d) High forearc subsidence leads to the drowning of shallow-water carbonate factories and return to deep-water, pre-collisional levels. The trailing edge of the bathymetric feature sustains volcanic quiescence due its ongoing subduction in the window of major slab dehydration. (e) Subduction of normal oceanic crust in the window of major slab dehydration leads to renewed volcanic arc activity, which results in deep-water volcaniclastic sedimentation. Small-sized shallow-water carbonate factories may establish in areas sheltered from the detrital input derived from active volcanoes.



1224

1225 **Figure 3.** (a) Detailed geological map of the inner Tempisque Forearc Basin showing the outcrops of
 1226 the Barra Honda Formation (in blue) and its stratigraphic substratum (modified after Flores et al., 2003a,
 1227 2003b; Denyer et al., 2014b; Baumgartner-Mora & Baumgartner, 2016). (b) Geological map of the
 1228 Nicoya town area (modified after Denyer et al., 2014b). The studied road and quarry sections of the
 1229 upper Barra Honda Formation are indicated.

1230

1231

1232

1233

1234

1235

1236

1237

1238

1239

1240

1241

1242

1243

1244

1245

1246

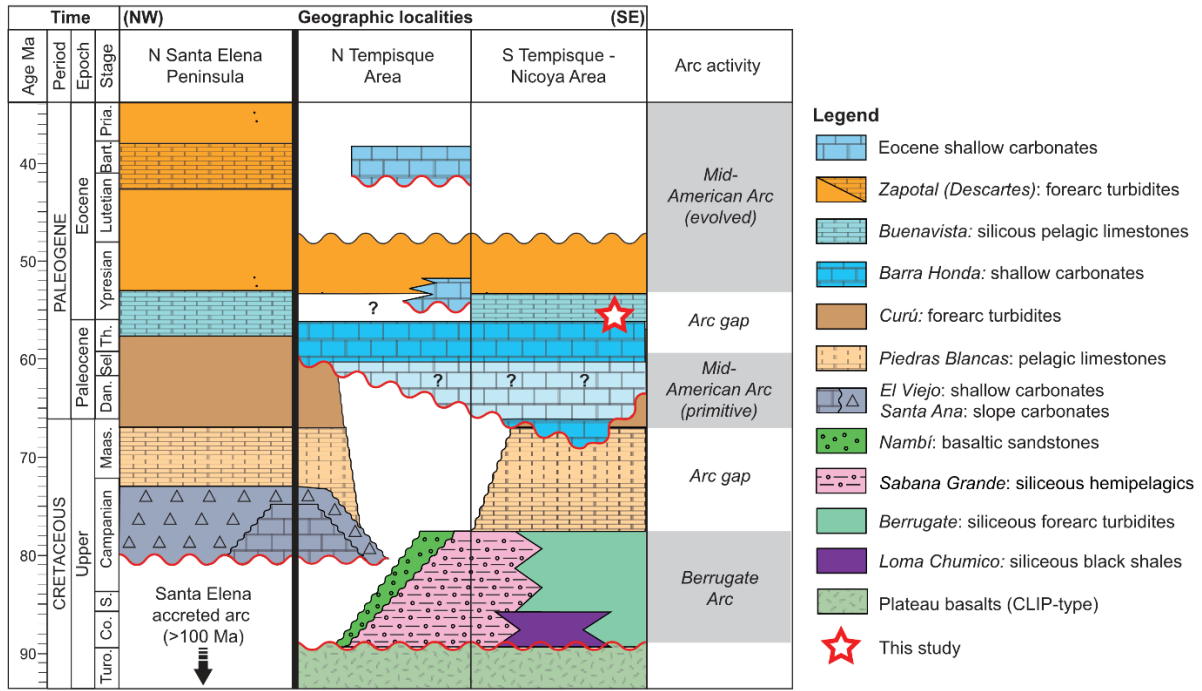
1247

1248

1249

1250

1251



1252

1253 **Figure 4.** Chronostratigraphic logs of the Tempisque-Nicoya and northern Santa Elena areas (adapted
 1254 from Baumgartner-Mora & Baumgartner, 2016; based on data from Baumgartner et al., 1984; Bandini
 1255 et al., 2008; Denyer et al., 2014a, 2014b; Andjić et al., 2016, 2018a, 2019a). Formation names are
 1256 indicated in italics. Major unconformities are marked with red wavy lines. White areas are stratigraphic
 1257 gaps due to erosion or non-deposition. Light blue fields with question marks represent temporal
 1258 uncertainties of stratigraphic gaps. Two successive arc systems are recorded by the forearc
 1259 sedimentation: the Berrugate Arc, restricted to the Manzanillo Terrane precedes the docking of the
 1260 Santa Elena and Nicoya Terranes, while the Mid-American Arc produced forearc sediments in the
 1261 overlap sequences of the three terranes (see Figure 1b for a terrane map). A temporary arc gap is
 1262 documented by the Barra Honda carbonate shoal and the distal, overlying pelagic Buenavista Fm.

1263

1264

1265

1266

1267

1268

1269

1270

1271

1272

1273

1274

1275

1276

1277

1278

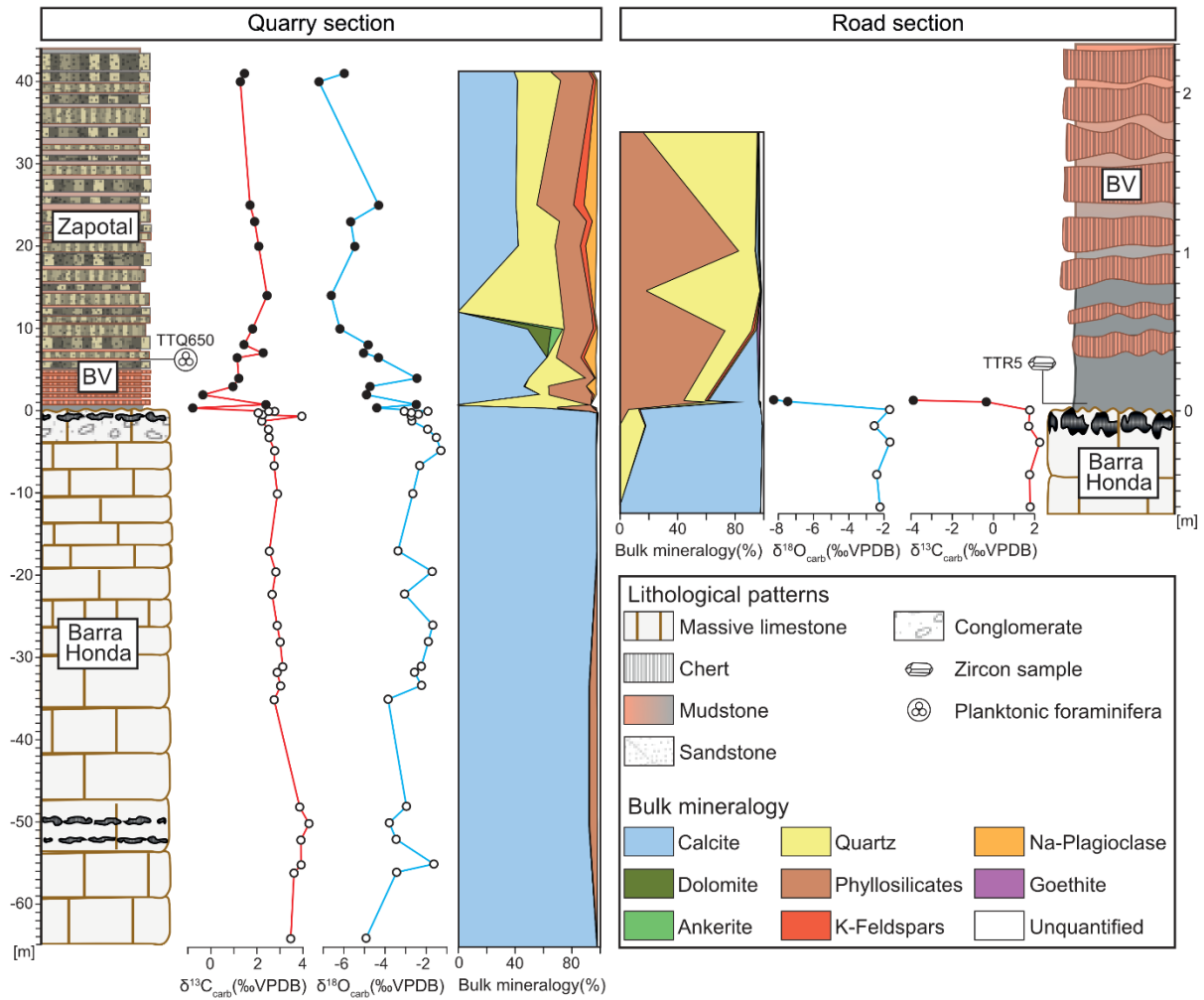
1279

1280

1281

1282

1283



1284

1285 **Figure 5.** Lithological logs, stable isotope compositions, and bulk rock mineralogy of the quarry and
 1286 road sections of the upper Barra Honda Formation in the Teresita quarry. BV = Buenavista Formation.

1287

1288

1289

1290

1291

1292

1293

1294

1295

1296

1297

1298

1299

1300

1301

1302

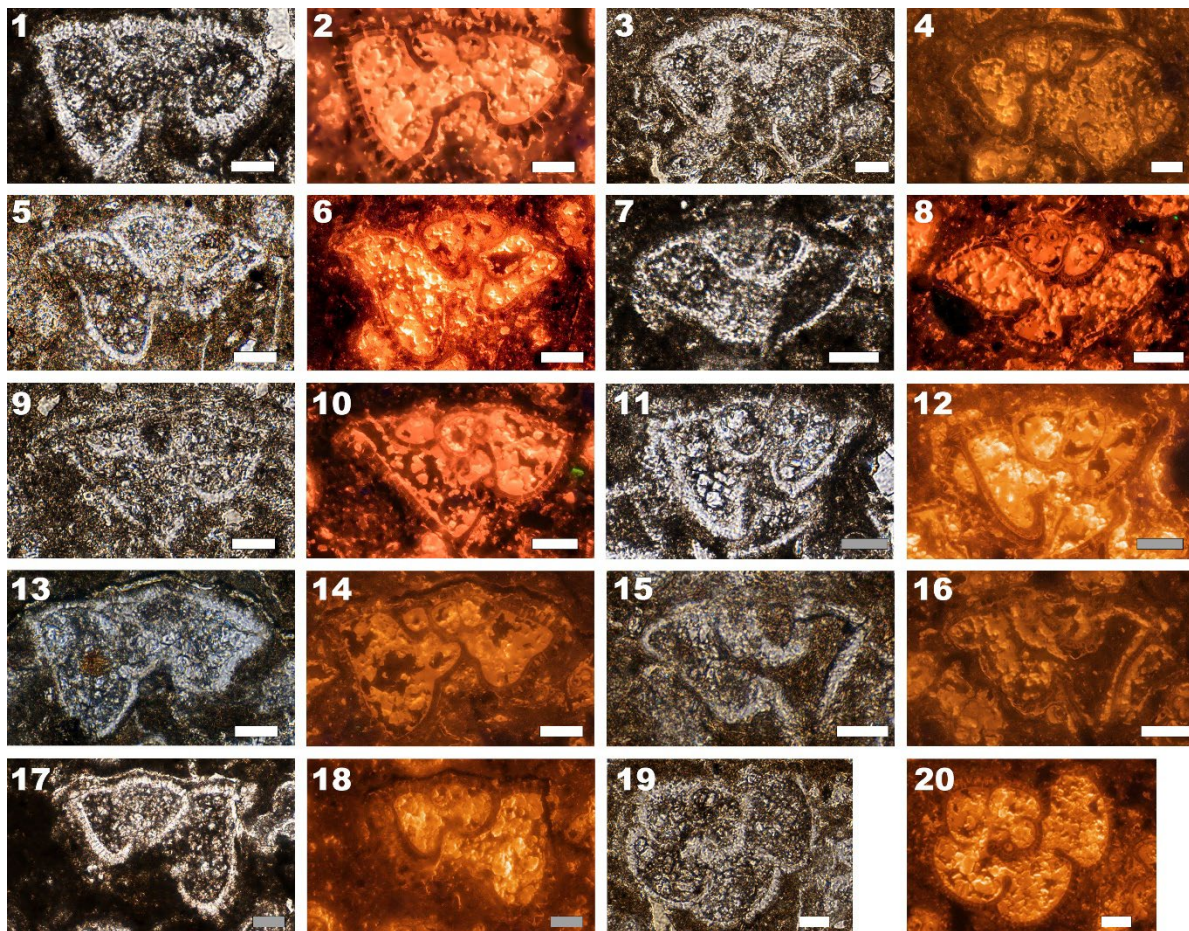
1303

1304

1305

1306

1307



1308

1309 **Figure 6.** Planktonic foraminifera from the Buenavista Formation (sample TTQ650; quarry section).
 1310 White scale bars are 50 μm and gray scale bars are 200 μm (11, 12, 17, 18). 1, 2,
 1311 *Acarinina* cf. *quetra* (top E3-E6). 3, 4, *Morozovella* cf. *formosa*. 5, 6, *Morozovella gracilis* (P5-E5). 7,
 1312 8, *Planorotalites pseudoscitula* (P5-E7). 9–12, *Morozovella subbotinae* (P5-E5). 13–16, *Morozovella*
 1313 *aequa* (P4c-E5). 17, 18, *Morozovella* cf. *lensiformis*. 19, 20, *Acarinina angulosa* (P5-E7). The
 1314 concurrent range of these taxa is from top E3 to E5 Zones (early to middle Ypresian age).

1315

1316

1317

1318

1319

1320

1321

1322

1323

1324

1325

1326

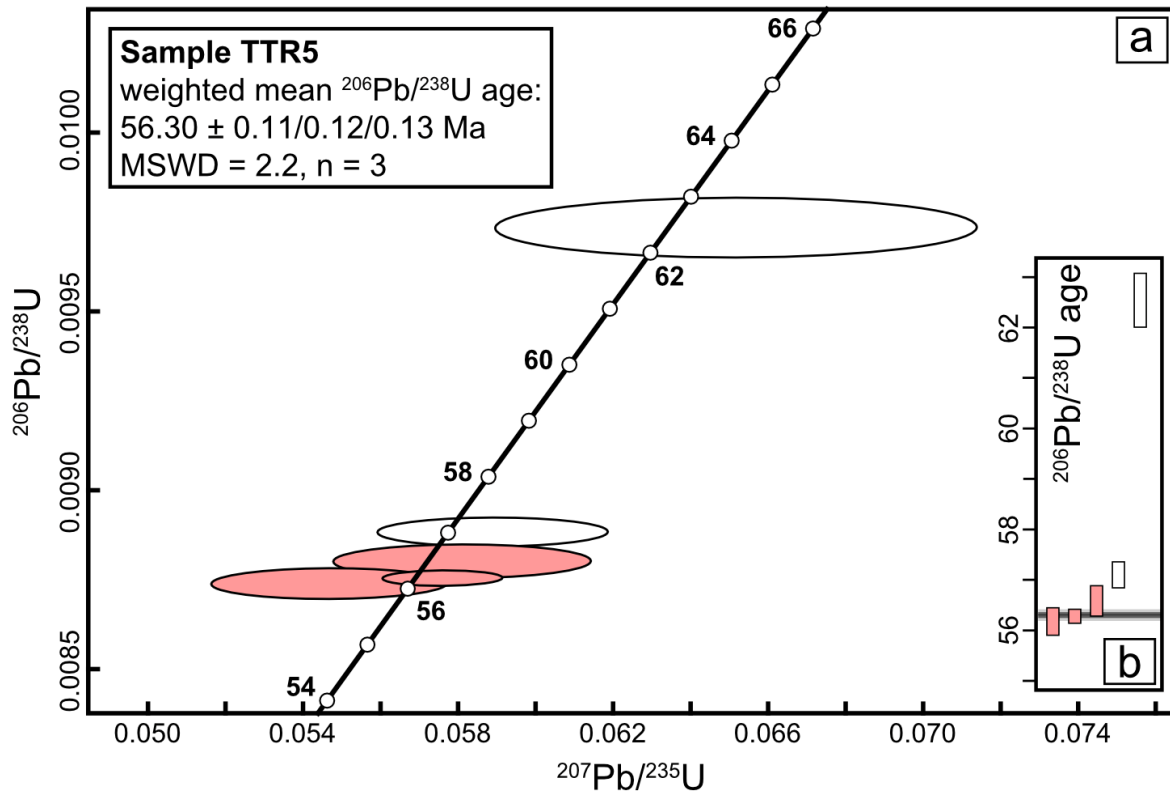
1327

1328

1329

1330

1331



1332

1333 **Figure 7.** CA-ID-TIMS U–Pb dates for sample TTR5 (lowermost Buenavista Formation; road section).
 1334 (a) The concordia curve is drawn as a continuous black line. Bold numbers are concordant dates (Ma).
 1335 Error ellipses are drawn at the 2σ confidence level. Reddish and white error ellipses represent data
 1336 points included in and excluded from the weighted mean $^{206}\text{Pb}/^{238}\text{U}$ date calculation, respectively. (b)
 1337 Ranked single-grain $^{206}\text{Pb}/^{238}\text{U}$ dates. Box heights representing date uncertainties are drawn at the 2σ
 1338 confidence level. The horizontal grey band represents the uncertainty of the weighted mean $^{206}\text{Pb}/^{238}\text{U}$
 1339 date calculation (95 % confidence).

1340

1341

1342

1343

1344

1345

1346

1347

1348

1349

1350

1351

1352

1353

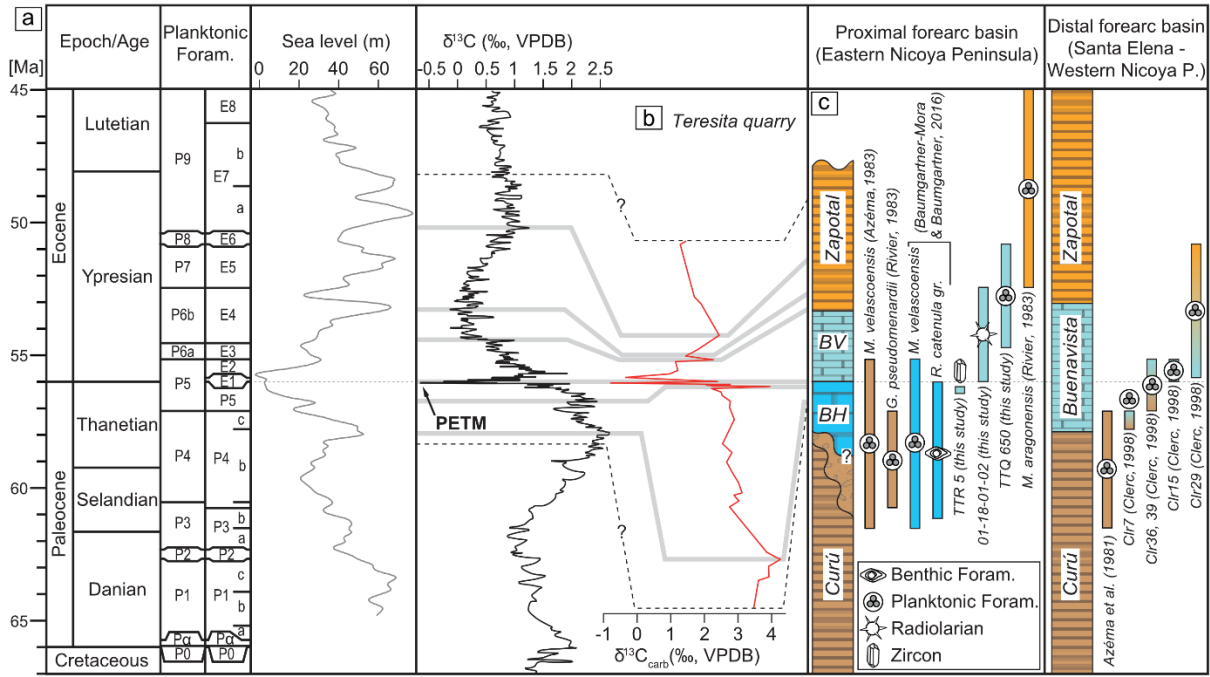
1354

1355

1356

1357

1358

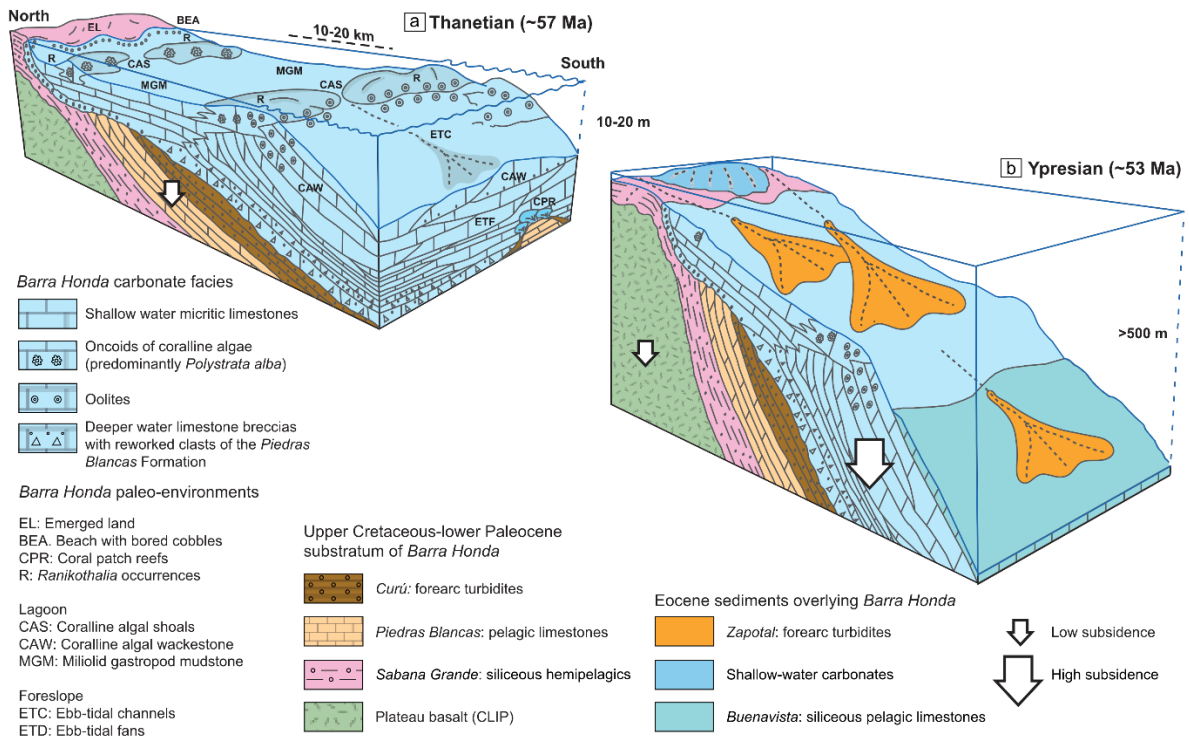


1359

1360 **Figure 8.** (a) Planktonic foraminifera biozonations (left column: Berggren et al., 1995; right column;
 1361 Pearson et al., 2006) and global carbon isotope curve (see Speijer et al., 2020 and references herein)
 1362 combined with the global mean sea level curve (Miller et al., 2020). Foram. = Foraminifera; PETM =
 1363 Paleocene–Eocene Thermal Maximum. (b) $\delta^{13}\text{C}_{\text{carb}}$ curve from the quarry section of the Teresita quarry
 1364 (this study). The grey lines tentatively correlate peaks of our new curve with those of the global carbon
 1365 isotope curve. (c) Simplified chronostratigraphic logs of the Tempisque-Nicoya and northern Santa
 1366 Elena areas combined with new and previous age constraints. The detailed explanation of previous
 1367 biostratigraphic constraints is given in Appendix A. BH = upper Barra Honda Formation; BV =
 1368 Buenavista Formation; P = Peninsula.

1369
 1370
 1371
 1372
 1373
 1374
 1375
 1376
 1377
 1378
 1379
 1380
 1381
 1382
 1383
 1384
 1385
 1386
 1387
 1388
 1389
 1390

1391



1392

1393 **Figure 9.** (a) Depositional model of the Barra Honda carbonate shoal during the Thanetian (modified
 1394 after Baumgartner-Mora & Baumgartner, 2016). Towards the south, Barra Honda limestone breccias
 1395 encroach on Curú forearc turbidites in an offshore environment and rework lithoclasts from the
 1396 underlying erosional surface cutting into older formations (Sabana Grande, Piedras Blancas, and Curú).
 1397 Upsection, massive intraclast breccias give way to platform sediments organized in ebb-tidal fans
 1398 (ETF). Towards the north, Barra Honda lagoonal micritic facies (MGM) progressively onlap on higher-
 1399 energy beach and foreshore sediments (BEA) on the eroded structural high during relative sea level rise
 1400 (i.e., low subsidence). The higher stratigraphic levels of Barra Honda show patchy shoals of coralgal
 1401 oncoïd grain- and packstones (CAS) with *Ranikothalia* sp. (R) and locally oolites. Rare coral patch
 1402 reefs (CPR) formed during the Maastrichtian in the lowermost stratigraphic levels of the Barra Honda
 1403 Formation. (b) View of the forearc basin 3 Ma after the demise of the Barra Honda carbonate shoal.
 1404 High forearc subsidence caused deepening of the basin floor to bathyal depths, preventing renewed
 1405 shallow carbonate production in the Barra Honda carbonate shoal after the PETM (56 Ma). Shallow
 1406 carbonate deposition may occur only on tectonic highs sheltered from detrital input.

1407

1408

1409

1410

1411

1412

1413

1414

1415

1416

1417

1418

1419

1420 **Appendix A: Paleocene–lower Eocene biochronologic framework**

1421

1422 The Paleogene, predominantly detrital formations of northern Costa Rica have been dated by means of
1423 occasional occurrences of planktonic and benthic foraminifera by several authors (Zoppis & Del
1424 Giudice, 1958; Dengo, 1962; Weyl, 1980; Azéma et al., 1981; Rivier, 1983; Baumgartner et al., 1984;
1425 Sprechmann, 1984). The existing fossil data of the Nicoya Peninsula was compiled by Denyer et al.
1426 (2014a, 2014b). Unfortunately, for most of this classical work, neither precise sample localities, nor
1427 illustrations of the reported fossils were provided, rendering precise biochronologic correlation difficult.
1428 More recently, published and unpublished, illustrated reports of microfossils in a more precise
1429 lithostratigraphic context have appeared, that are reviewed here for a biochronologic framework of the
1430 Paleocene–early Eocene time interval.

1431

1432 *Curú Formation: upper Maastrichtian to upper Paleocene forearc turbidites*

1433

1434 The Curú Fm. (= Rivas Fm. in Nicaragua), originally defined as “Formación Arenisca-Lutita Barco
1435 Quebrado” by Baumgartner et al. (1984) conformably overlies the upper Campanian–lower
1436 Maastrichtian pelagic Piedras Blancas Fm. (Flores et al., 2003a; Figures 1b, 3, and 4). It marks the
1437 beginning of detrital forearc sedimentation in the Tempisque (northern Costa Rica) and southern
1438 Sandino (southern Nicaragua) basins with distal turbidites of mainly basaltic composition (Lundberg,
1439 1982; Baumgartner et al., 1984; Astorga, 1987, 1988). Here, we re-evaluate the biochronologic age of
1440 the top of this formation in the Tempisque, Samara and Santa Elena areas.

1441

1442 While the lower part of the Curú Fm. is well-dated as late Maastrichtian by numerous mentions of
1443 globotruncanids, its top is poorly dated in the Nicoya Peninsula. In part, this is probably because it
1444 became partly or totally eroded (or never deposited?) beneath the unconformable base of the Barra
1445 Honda Fm. (Figure 4). On the other hand, the upper portion of the Curú Fm., the Cerco de Piedra Mb.
1446 (Sprechmann, 1982; Flores et al., 2003b) represents a coarsening and thickening megasequence
1447 (Baumgartner et al., 1984) that culminates in megaconglomerates containing Barra Honda-type
1448 boulders in its upper part. This facies is present in the area of Samara-Punta Indio and the Colorado de
1449 Abangares area (Denyer et al., 2014a), which is located southeast of the Barra Honda outcrops. The
1450 well-rounded conglomerates with up to m-sized boulders document subaerial erosion of basaltic to
1451 andesitic primitive island arc rocks (Patino et al., 2004), of tholeiitic basalts derived from the
1452 Manzanillo Terrane basement, and of overlying Upper Cretaceous formations, as well as possibly early
1453 parts of the Barra Honda Fm. Rivier (1983) dated this conglomerate as middle to late Paleocene based
1454 on its stratigraphic position and the occurrence of *Globanomalina pseudomenardii* (P4 Zone, middle
1455 Selandian–early Thanetian) near the top of the member. *Morozovella* gr. *velascoensis* is also reported
1456 by Azéma (pers. comm. 1983) in both the upper Curú Fm. and the overlying Buenavista Fm. of the
1457 Samara area.

1458

1459 In the Santa Elena area, the top of the Curú Fm. is transitional with the Buenavista Fm. and was
1460 examined by Azéma et al. (1981) and a more recent thesis by Clerc (1998). Azéma et al. (1981) dated
1461 the upper Curú Fm. in the area of Guajiniquil (Santa Elena area, Figure 1b) by the presence of
1462 *Morozovella velascoensis* (P3b-E2 Zones), *Subbotina triloculinoides* (P1b-P4 Zones), and
1463 *Globanomalina ehrenbergi* (P2-P4 Zones) resulting in a concurrent range of P3b-P4 Zones (middle
1464 Selandian–late Thanetian).

1465

1466 The sample Clr7 is located at the base of the section “Bahia Santa Elena” of Clerc (1998, approximately
1467 at 10°55'56"N, 85°48'57"W) in a dark colored thin-bedded limestone interbedded with arkosic turbidites
1468 and overlain by thin-bedded cherty limestone. It is here interpreted as the transition from the Curú Fm.
1469 to the Buenavista Fm. It contains *Acarinina mackannai* (P4a-P4c Zones), *Globanomalina imitata* (P1-
1470 P4c Zones), *Morozovella acuta* (P4b-E2 Zones), *Morozovella aequa* (P4c-E6 Zones), *Morozovella*

1471 *subbotinae* (P4c-E6 Zones), and *Morozovella velascoensis* (P3b-E2 Zones), which have a concurrent
1472 range of P4c (middle Thanetian).

1473

1474 Samples Clr36 and Clr39 are located in the middle and upper part of the “Bahia Blanca” section (Clerc
1475 1998, approximately at 10°56'41"N, 85°52'33"W). This section was attributed to the Buenavista Fm.
1476 by Clerc (1998) but was mapped as upper Curú Fm. by Andjić et al. (2016) because of the fact that the
1477 section contains rather mafic detrital sediments and only rare hemipelagic intervals; in the most recent
1478 maps of the Santa Elena Peninsula, Denyer (2019) considered Buenavista-type siliceous carbonates as
1479 part of the lowermost Brito Fm. The samples contain: *Globanomalina chapmani* (P4-base E4 Zones),
1480 *Morozovella aequa* (P4c-E5 Zones), *Morozovella velascoensis* (P3b-E2), *Morozovella subbotinae* (P5-
1481 E5), *Morozovella acuta* (P4-E2 Zones), *Globanomalina luxorensis* (P5-E2 Zones) and *Subbotina* spp.,
1482 which gives a concurrent range of P5-E2 Zones (late Thanetian–early Ypresian).

1483

1484 In summary, the transitional top of the Curú Fm. to the Buenavista Fm. can be dated in the northern
1485 Santa Elena area as late Thanetian–early Ypresian. In the Nicoya area, the Curú Fm. is either
1486 conformably overlain by the Descartes Fm. (see below), or partly eroded (or lacking), or represented
1487 by the Cerco de Piedra Conglomerate of possible middle Selandian to early Thanetian age. The presence
1488 of Barra Honda clasts in this conglomerate implies that the Barra Honda carbonate shoal started to
1489 develop at least since the early Thanetian and is therefore partly coeval with the upper Curú Fm. (see
1490 also Andjić et al., 2016).

1491

1492 *Barra Honda Formation: Uppermost Cretaceous(?)–Thanetian carbonate shoal*

1493

1494 The occurrence of *Ranikothalia* gr. *catenula* in the lowermost beds of the upper Barra Honda Fm. at
1495 Cerro Espiritu Santo (Figure 3a) is one of the rare biostratigraphic markers in the formation.
1496 Baumgartner-Mora and Baumgartner (2016) have largely discussed the age range of *Ranikothalia* gr.
1497 *catenula*, which still has uncertainties. The best calibration of its first appearance was proposed by
1498 Robinson and Wright (1993), who restricted *R. catenula* to the late Paleocene, based on independent
1499 dating of its first appearance by nannofossils (NP5-7 Zones, according to Jiang & Robinson, 1987),
1500 which corresponds to the middle Selandian–early Thanetian (middle P3b to upper part of P4b Zones;
1501 Speijer et al., 2020). This is probably the maximum age of upper Barra Honda in its northernmost
1502 sections. Danian-lower Selandian macro- and microfossils are rare in shallow carbonates and have not
1503 been found in any Barra Honda facies. The transition from lower “Puerto Nispero” to upper Barra
1504 Honda sections cannot be observed and could be a stratigraphic gap due to emersion during an eustatic
1505 sea-level low during the latest Cretaceous-Danian (Miller et al., 2005).

1506

1507 The top of Barra Honda Fm. can be dated by the occurrence of *Morozovella velascoensis* that occur in
1508 several outcrops in the upper part of the formation with open marine influence (Baumgartner-Mora &
1509 Baumgartner, 2016). This planktonic foraminifera goes extinct about 0.2 Ma to 1 Ma after the
1510 isotopically defined Paleocene–Eocene boundary (Pak & Miller, 1992; Kelly et al., 1998; Molina et al.,
1511 1999; Arenillas et al., 1999). Hence, the minimum age of the Barra Honda Fm. is likely to be latest
1512 Paleocene or earliest Eocene. It must be in part coeval with the basinal, lower part of the Buenavista
1513 Fm. outcropping in the Santa Elena Peninsula (Figures 1b and 4).

1514

1515 *Buenavista Formation: upper Paleocene to lower Eocene pelagic cherty limestones and tuffaceous*
1516 *mudstones*

1517

1518 Originally described by Baumgartner et al. (1984) in the Samara area and reported from the Santa Elena
1519 area, this formation was later ignored and included with the Zapotal Mb., the basal part of the Descartes
1520 Fm. It is coeval and most probably a lateral, more distal, equivalent of the lowest part of the Zapotal
1521 Mb. (*sensu* Denyer et al., 2014a). In contrast with the Zapotal Mb., this formation is largely pelagic to

1522 tuffaceous-hemipelagic and lacks coarse detrital turbidites. Abundant planktonic foraminifera and
1523 radiolarians allow precise dating of this short-lived stratigraphic interval.

1524

1525 In the type locality (Playa Buenavista, Samara area), the Buenavista Fm. was dated by Baumgartner et
1526 al. (1984) as late Paleocene–early Eocene, principally based on the recognition of *Morozovella* gr.
1527 *velascoensis*. In the Santa Elena area, the Buenavista Fm. was dated in several sections measured by
1528 Clerc (1998). Sample Clr15 is located in the middle of the “Bahia Santa Elena” section (Clerc, 1998;
1529 approximately at 10°56'4"N, 85°48'43"W) at the base of a faulted interval of thin-bedded siliceous
1530 limestones interbedded with abundant marls. It contains *Subbotina* sp., *Morozovella velascoensis* (P3b-
1531 E2 Zones), *Morozovella subbotinae* (P5-E5 Zones), *Morozovella aequa* (P4c-E6 Zones), *Morozovella*
1532 *acuta* (P4b-E2 Zones), *Globanomalina chapmani* (P3-base E4 Zones), *Acarinina pseudotopilensis* (E1-
1533 E7 Zones), and *Acarinina mckannai* (P4a-P4c Zones, possibly reworked), which gives a consistent
1534 concurrent range of E1-E2 Zones (late Thanetian–early Ypresian). This sample suggests that part of the
1535 Buenavista Fm. is at least late Thanetian in age. Sample Clr 24 is located at the top of the “Bahia Santa
1536 Elena” section (Clerc, 1998; approximately at 10°56'8"N, 85°48'38"W), which corresponds to the
1537 middle or upper part of the Buenavista Fm. It contains *Morozovella subbotinae* (P5-E5 Zones) and
1538 *Subbotina* sp. (P5-E5 Zones), which suggests a late Thanetian–middle Ypresian age. Sample Clr29 is
1539 located near the top of the “Isla Los Cabros” section (Clerc, 1998; approximately at 10°56'31"N,
1540 85°48'58"W). It represents the transition between the Buenavista and the Descartes formations and
1541 contains *Pseudohastigerina* sp. (first appearance: E2 Zones), *Morozovella subbotinae* (P5-E5 Zones),
1542 which gives a range of E2-E5 Zones (early–middle Ypresian).

1543

1544 In summary, the Buenavista Fm. has an overall middle–late Thanetian to early Ypresian age. In the
1545 Santa Elena area the total age range of the formation is represented. In contrast, the lower Ypresian part
1546 of this formation overlies the Barra Honda Fm. in the Teresita quarry, as shown in section 5.2, where a
1547 new assemblage of planktonic foraminifera is described.

1548

1549 *Zapotal Member (Descartes Formation): Eocene forearc turbidites*

1550

1551 The Zapotal Mb. corresponds to a succession of siliceous and carbonate-bearing volcanoclastic
1552 turbidites of up to 2 km in thickness (Rivier, 1983; Astorga, 1987; Flores et al., 2003a). Rivier (1983)
1553 reported early to middle Eocene planktonic foraminifera from the Zapotal Mb.: *Morozovella gracilis*
1554 (P5-E5 Zones), *Morozovella formosa* (E4-E6 Zones), *Morozovella aragonensis* (E5-E9 Zones). In
1555 section 4.2., we re-evaluate a radiolarian assemblage reported by Bandini et al. (2008) from the Zapotal
1556 Mb.

1557

1558